



# Dynamics of P-binding forms in sediments of a mesotrophic hard-water lake: Insights from non-steady state reactive-transport modeling, sensitivity and identifiability analysis



Jalene McCulloch<sup>1</sup>, Alex Gudimov<sup>1</sup>, George Arhonditsis, Alexey Chesnyuk, Maria Dittrich<sup>\*</sup>

Department of Physical and Environmental Sciences, University of Toronto Scarborough, 1265 Military Trail, Toronto M1C 1A4, Canada

## ARTICLE INFO

### Article history:

Received 6 November 2012

Received in revised form 10 June 2013

Accepted 11 June 2013

Available online 26 June 2013

Editor: Carla M. Koretsky

### Keywords:

Phosphorus

Lake sediments

Reaction-transport model

Early diagenesis

Phosphorus binding forms

Lake Simcoe

## ABSTRACT

Sediments can act both as a source or sink of contaminants and nutrients in lakes. In this study, we developed a non-steady state reactive transport diagenetic model to gain insights into the dynamics of phosphorus binding forms in the sediments of Lake Simcoe, a mesotrophic hard-water lake located in Southern Ontario, Canada. We investigate three basins of the lake with differences in their phosphorus binding forms, reflecting the distinct spatiotemporal patterns of land use and urbanization levels in the watershed. In the model, total phosphorus is divided into loosely adsorbed phosphorus, phosphorus bound with aluminum, organic phosphorus, redox sensitive and apatite phosphorus, and dissolved phosphorus in pore water. Using the fluxes of organic and inorganic matter along with the concentrations of dissolved substances as dynamic boundary conditions, we simulated the depth profiles of sixteen solute and solid components. The model closely reproduced the fractionation data of phosphorus binding forms. The impact of the interplay between sedimentation fluxes and geochemical conditions on phosphorus diagenesis was then studied under a range of anthropogenic disturbances and natural variability in Lake Simcoe. We also conducted sensitivity analysis that pinpointed the most influential processes underlying the mechanistic foundation of the model. The non-steady state diagenesis model reveals that apatite P dominates the P forms in Cook's Bay, which has been overwhelmingly influenced by agricultural activities in the corresponding watershed during the last 100 years. In contrast, Kempenfelt Bay has been primarily impacted by urbanization and experienced oxygen depletion in the deep water. Thus, we found that organic P binding forms dominated over redox sensitive P when urban loading was intensified. Finally, our study offers insights into the identifiability of the model as well as into the factors that will be critical to monitor in order to improve its credibility. The model outputs are sensitive to the concentrations of dissolved oxygen and pH at the sediment–water interface. The sensitivity with respect to these factors overwhelmingly dominates over all other parameters. Furthermore, the characterization of the sedimentation fluxes; namely, the composition of settling organic matter, expressed as the ratio of degradable to inert organic matter is the second strongest factor that can influence the inference drawn by our modeling exercise.

Crown Copyright © 2013 Published by Elsevier B.V. All rights reserved.

## 1. Introduction

Phosphorus (P) is the typical limiting macronutrient for the growth of primary producers in freshwater ecosystems, and the mechanisms that affect P bioavailability in the water column are well studied (Wetzel, 2001; Schindler et al., 2008; Carey and Rydin, 2011). In many catchments, P loads that originate from human activities exceed natural loading by several orders of magnitude (Falkowski et al., 2000). The anthropogenic P sources can be distinguished into (i) point sources, especially effluents from waste water treatment plants; and (ii) diffuse or non-point sources, usually associated with agricultural activities

(Schippers et al., 2006). The level of exogenous P loading is causally linked with the manifestation of eutrophication phenomena, such as excessive algal growth, poor water clarity, taste and odor problems, hypolimnetic oxygen depletion, and subsequently a decrease in the recruitment of coldwater fish in deep stratified lakes (Evans, 2007). Thus, the main focus of lake restoration projects usually revolves around the control of external point and non-point sources of nutrient loading.

However, lake sediments act either as a sink or source of a large number of organic and inorganic compounds including phosphorus in the form of readily bioavailable phosphates. When acting as a P source, lake sediments can considerably increase the water column concentrations and thus modulate the severity of eutrophication regardless of the level of external forcing (Nürnberg, 2009; Smith et al., 2011). In general, the release of P from lake sediments (or internal loading) is caused by a suite of physical, chemical, and biological processes such as: desorption,

<sup>\*</sup> Corresponding author. Tel.: +1 416 208 2786; fax: +1 416 287 7279.

E-mail address: [mdittrich@utsc.utoronto.ca](mailto:mdittrich@utsc.utoronto.ca) (M. Dittrich).

<sup>1</sup> Authors contributed equally.

ligand exchange mechanisms, dissolution of precipitates, mineralization processes, release from living cells, and autolysis of cells (Kleeberg and Kozerski, 1997; Hupfer and Lewandowski, 2008). Other environmental factors related to the P release from the sediments include temperature, pH, redox potential (Eh), hydraulic conditions, nitrate and sulfate concentrations, bioturbation, and other biological activities (e.g., Rydin, 2000; Gao et al., 2005; Zhou et al., 2005; Christophoridis and Fytianos, 2006). Consequently, the potential of P in the sediments to become a significant driving force is related to the conditions under which it can be immobilized or released. Such information can be provided from the various P binding forms, such as the loosely adsorbed labile P, redox sensitive FeOOH bound P, P bound to hydrated oxides of Al or Fe, calcium carbonate bound P (apatite P), and organic P (Psenner and Pusco, 1988), see also the review by Lukkari et al. (2007). The predominance of different P binding forms offers insights into the degree of system susceptibility to internal loading (Bostrom et al., 1988; Nürnberg, 1988; Kopacek et al., 2005). However, despite the considerable efforts to elucidate sediment response to changes in exogenous P loading, we still do not fully understand the underlying ecological mechanisms that ultimately mediate the duration and extent of P release (cf. Lewis et al., 2007).

In this regard, dynamic modeling of P binding forms in the sediment can provide critical support for water quality managers in developing appropriate scenarios regarding the “if”, “how”, and to “what extent” internal loading will impact P concentrations in lakes (see Lewis et al., 2007). Diagenesis modeling implements non-steady state transport reactive processes based upon partial differential equations for organic matter decomposition, geochemical transformations between solid and dissolved components along with biological activities coupled with the physical processes of diffusion, compaction, and advection (Boudreau, 1997; Dittrich et al., 2009; Couture et al., 2010; Reed et al., 2011b). This family of models can shed light onto crucial diagenesis processes that are extremely difficult to measure in-situ. A characteristic example is the recent analysis of the long-term development of hypoxia in deep waters and its impact on sediment properties, such as sapropel and iron-bounded P in Mediterranean and Baltic Sea sediments (Reed et al., 2011a,b). Diagenetic modeling has also been applied to quantify pathways of organic matter degradation from anoxic lake sediments (Lopes et al., 2010) and FeS accumulation in deep stratified lakes (Dittrich et al., 2009). However, limited attempts have been made to achieve dynamic predictions of sediment P release and immobilization, and even rarer is the technical analysis of the most sensitive parameters/processes that are directly linked to the model's predictive capacity and structural uncertainty.

In this study, we calibrate and subsequently validate a dynamic transport–reaction, diagenetic model which simulates depth profiles of P binding forms with Fe, Al and apatite, organic carbon, solid iron, calcium and manganese sediment content as well as the levels of dissolved compounds, such as oxygen, nitrogen, pH and phosphorus. Our case study is the Lake Simcoe, a mesotrophic hard-water system located in Southern Ontario, Canada. We investigate three basins of the lake with differences in their land use patterns, urbanization levels, and loading history (Gudimov et al., 2012). We present results on simulated depth profiles of dissolved P as well as P binding forms, and their seasonal and long-term dynamics in conjunction with the external loading rates and oxygen concentrations at the sediment–water interface over the past 400 years. Our paper also illustrates a framework for parameter sensitivity and identifiability analysis. The parameters examined describe a wide range of biogeochemical processes, such as organic matter degradation, bioirrigation and bioturbation, precipitation and dissolution of minerals, adsorption and P transformations. Our analysis aims to address several important research questions, such as: Can phosphorus retention in lake sediments be predicted based on sediment mineralogy, sedimentation substance inputs, catchment type, and other characteristics? How sediment retention capacity with respect to phosphorus may respond to changes caused by human activities? What are

the uncertainties in diagenetic model predictions and how many parameters are uniquely identifiable?

## 2. Material and methods

### 2.1. Study site

Lake Simcoe is the 5th largest lake in the southern part of the Province of Ontario with some 400,000 people living in its 3572 km<sup>2</sup> watershed. Lake Simcoe has a surface area of 722 km<sup>2</sup> with a maximum and mean depth of 41.5 m and 14.2 m, respectively. It is a glacially formed, hard-water dimictic lake with a flushing time of approximately 13 years. The Lake Simcoe area was glaciated by the Laurentide Ice Sheet with predominantly south to southwest ice flow (Todd et al., 2008). Mean depths of modern sediments are 3.4 m in Kempenfelt Bay and the Main Basin and 2.2 m in Cook's Bay (Johnson and Nicholls, 1989). Although ongoing research in Lake Simcoe has provided considerable insights into the interplay between external P loading and ambient water quality conditions (Palmer et al., 2011; Young et al., 2011), there is a lack of understanding of the role that sediments play in the lake P budget, while the actual mechanisms of P internal loading is a matter of controversy (Hiriart-Baer et al., 2011). Water quality modeling suggests that there is significant variability of TP and chlorophyll *a* in space and time, but we do not know to what extent this heterogeneity is modulated by the P release from the sediments (Gudimov et al., 2012).

Three different basins have been investigated in this study: Cook's Bay (C9), Kempenfelt Bay (K42) and the Main Basin (K45) (Fig. 1). These three basins have been chosen because they have undergone different loading histories (Hiriart-Baer et al., 2011; Landre et al., 2011). Hiriart-Baer et al. (2011) reports a twofold increase of the sedimentation rates in Cook's Bay relative to the rest of the lake due to an extension of the agricultural and urban land uses at the beginning of the 19th century. Loss of wetlands and the channelization of the lower Holland River in the 1930s caused a substantial increase of the sedimentation rates in Cook's Bay. In Kempenfelt Bay, the urbanization activities associated with the City of Barrie's population growth after the 1950s is responsible for the increased sedimentation rates (Hiriart-Baer et al., 2011). The Main Basin received a larger proportion of terrestrial organic matter, which is likely the result of erosion due to de-forestation, a main contributor to the sedimentation fluxes. The lake as a whole is considered to be a hard-water, mesotrophic, dimictic lake (MOE, 2010).

### 2.2. Model formulation

#### 2.2.1. Reactive-transport model

A 1-D non-steady state transport reactive model for sediment diagenesis of solid ( $X_i$ ) and dissolved ( $S_i$ ) substances was used in this study (Dittrich et al., 2009). The model accounts for the molecular diffusion of dissolved species (the molecular diffusion coefficient  $D_{S_i}$ ), velocities of sediment movement ( $v_{sed}$ ) due to sedimentation flux ( $f_{X_i}$ ), compaction of porosity  $\theta$  with depth ( $z$ ), bioturbation ( $D_B$ ) and biogeochemical transformation rates ( $r_{X_i}$  and  $r_{S_i}$ ) in time ( $t$ ). Briefly, the following differential equations have been implemented:

$$\frac{\partial(\theta S_i)}{\partial t} = \frac{\partial}{\partial z} \left( D_B \frac{\partial(\theta S_i)}{\partial z} + \theta D_{S_i} \frac{\partial S_i}{\partial z} \right) + r_{S_i} - \alpha_{bioirrig} * \theta * (S_i - S_i^{SWI}) \quad (1)$$

$$\frac{\partial X_i}{\partial t} = - \frac{\partial(v_{sed} X_i)}{\partial z} + \frac{\partial}{\partial z} \left( D_{B,X_i} \frac{\partial X_i}{\partial z} \right) + r_{X_i} \quad (2)$$

The boundary conditions for sediment–water interface,  $Z_{SWI}$  and the deepest sediment layer  $Z_{max}$ :

$$S_i(Z_{SWI}) = S_i^{SWI} \quad (3)$$

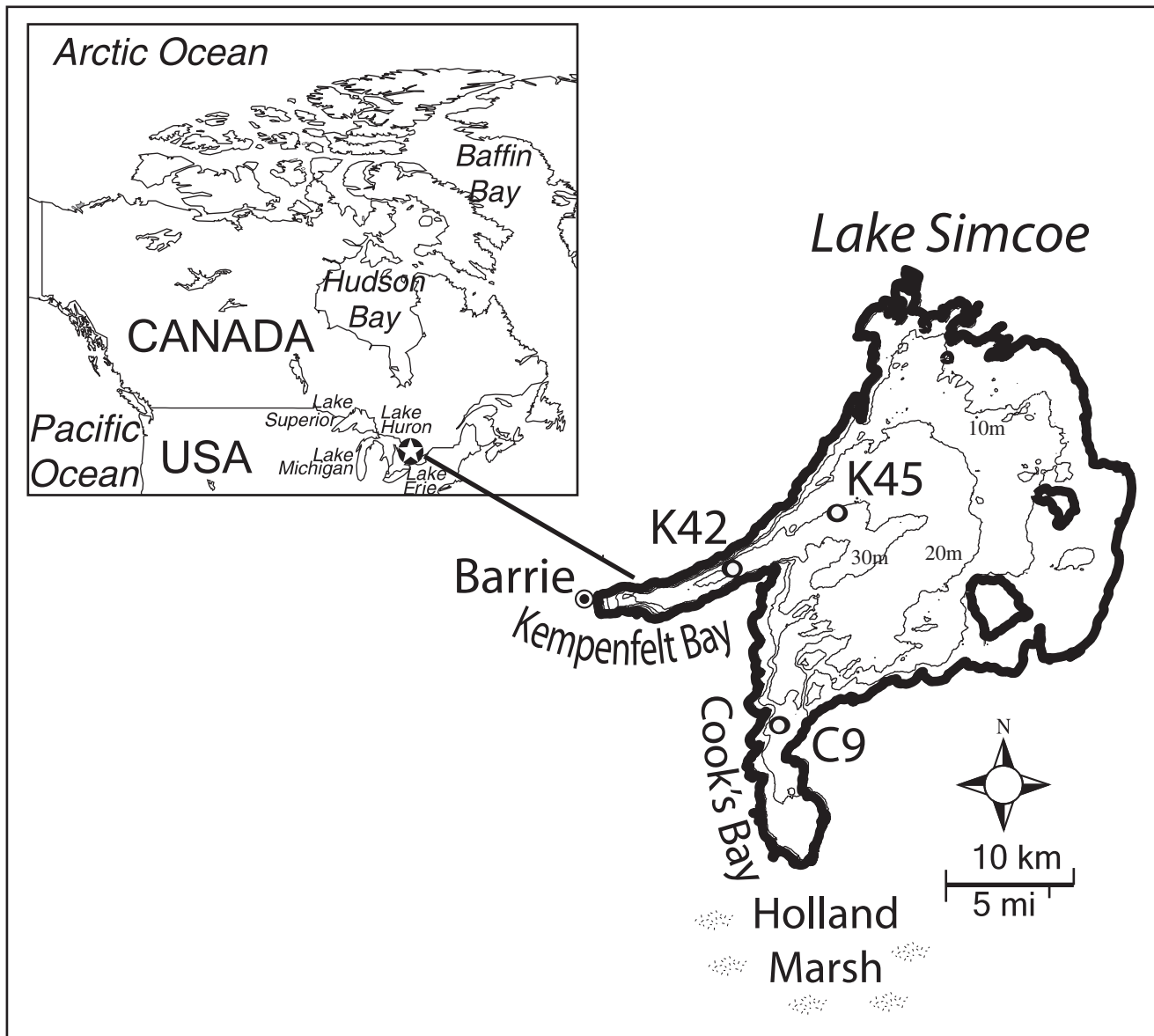


Fig. 1. Map of Lake Simcoe.

$$X_i(z_{SWI}) = \frac{f_{X_i}}{v_{sed}(z_{SWI})} \quad (4)$$

$$Q(z_{SWI}) = Q_{SWI} \quad (5)$$

$$\frac{\partial S_i}{\partial z}(z_{max}) = 0 \quad (6)$$

where  $S_i^{SWI}$  is the concentration of dissolved substance  $i$  in the water column at the sediment–water interface (SWI), and  $\theta_{SWI}$  is a porosity of newly deposited sediment at sediment–water interface surface  $z_{SWI}$ . In these equations,  $t$  is time,  $z$  is the depth coordinate within the sediment ( $z_{SWI} = 0$  at the sediment surface, positive downward orientation),  $S_i$  is the concentration of dissolved substance  $i$  in the sediment pore water (mass per pore water volume),  $\theta$  is the porosity of the sediment,  $\alpha_{Bioirrig}$  is a bioirrigation coefficient,  $D_{Si}$  is the molecular diffusion coefficient of dissolved substance  $i$ ,  $r_{Si}$  is the total transformation rate of dissolved substance  $i$  (mass per total sediment volume and time),  $X_i$  is the concentration of particulate substance  $i$  in the sediment (mass per total sediment volume),  $v_{sed}$  is the velocity

of movement of the solid phase of the sediment relative to a coordinate system with an origin at the sediment surface,  $D_{B,X_i}$  is the effective diffusion coefficient of particulate substance  $i$ ,  $r_{X_i}$  is the total transformation rate of particulate substance  $i$  (mass per total sediment volume and time),  $f_{X_i}$  is the sedimentation flux of particulate substance  $i$ ,  $X_i$  is the density of particulate substance  $i$  (mass per volume of particulate substance),  $z_{SWI} = 0$  is the  $z$  coordinate at the sediment surface,  $z_{max}$  is the  $z$  coordinate at the deepest point (equal to the thickness) of the sediment layer,  $S_{i,SWI}$  is the concentration of dissolved substance  $i$  in the water column at the sediment surface.

The modeled solid  $X_i$  and dissolved  $S_i$  species considered in the model along with the associated reaction rates are listed in Tables 1–3. The organic particles are represented by degradable and inert fractions with mass composition presented in Table 4. The other modeled solids aside from the P fractions are  $MnO_2$ ,  $FeOOH$ ,  $FeS$ ,  $CaCO_3$ ,  $FeCO_3$ ,  $MnCO_3$  and inorganic inert matter (see Table 1).

### 2.2.2. Reaction kinetics

The primary redox reactions for organic matter bacterial degradation (Table 2) are based on Monod kinetics with inhibition terms to account

**Table 1**  
State variables of the model.

| Dissolved components      | Solid components  |
|---------------------------|---|
| Oxygen                    | Inert organic matter:<br>$C_{\alpha C/12}H_{\alpha H}O_{\alpha O/16}N_{\alpha N/14}P_{\alpha P/31}S_{\alpha S/32}$      |
| Nitrate                   | Degradable organic matter:<br>$C_{\alpha C/12}H_{\alpha H}O_{\alpha O/16}N_{\alpha N/14}P_{\alpha P/31}S_{\alpha S/32}$ |
| Manganese                 | Manganese oxide   |
| Iron (II)                 | Anhydrous iron(III) oxide-hydroxide   |
| Ammonium and ammonia      | Manganese carbonate   |
| Calcium                   | Iron bound (redox sensitive) phosphorus   |
| Bicarbonate and carbonate | Calcium carbonate   |
| Dihydrogen phosphate      | Calcium bound phosphorus,<br>Aluminum bound phosphorus  |
| Monohydrogen phosphate    | Adsorbed phosphorus   |
| Hydrogen sulfide          | Siderite, iron sulfide  |
| Sulfide                   | Organic phosphorus  |
| Hydrogen and hydroxide    | Inorganic matter  |

for gradients in redox potential among oxidants (Van Cappellen and Gaillard, 1996). The modeled oxidants are oxygen, nitrate, manganese oxide, iron hydroxides and sulfate (PR1–5). The oxidation of ammonium, sulfide, Fe-hydroxides and -sulfides are also considered as secondary redox reactions (SR1–4). Mineral precipitation and dissolution for carbonates and iron sulfides are included in the model (MR1–4) as well as equilibrium conditions for carbonic acid and bicarbonate dissociation, ammonium dissociation, orthophosphate dissociation, and sulfide dissociation (ER1–7).

The model has been developed to study P transformations in and release from the sediments, especially the P binding forms derived by sequential fractionation. In this study, we used the phosphorus fractionation method from Psenner and Pusco (1988) as modified by Rydin (2000). The P forms separated with this sequential fractionation include loosely adsorbed (labile) P (extracted with  $NH_4Cl$ ,  $NH_4Cl$ -TP), redox-sensitive bound P (extracted with bicarbonate dithionite, BD-TP), P bound to hydrated oxides of aluminum or iron oxides (extracted with NaOH, NaOH-SRP), organic bound P (extracted with NaOH, NaOH-NRP), carbonates bound P (apatite P) (extracted with HCl, HCl-TP) and refractory P (Refract-P) (Psenner and Pusco, 1988). The

detailed description of the fractionation technique has been recently presented by Dittrich et al. (2013).

The phosphorus diagenesis model structure, depicted in Fig. 2, demonstrates the incorporation of these P fractions into the model along with the processes and relevant reaction rates considered. The advancement of our dynamic non-steady-state model is the incorporation of the formation of major phosphorus binding forms, i.e., adsorbed P ( $NH_4Cl$ -TP), redox-sensitive Fe–P (BD-TP), aluminum-bound P Al–P (NaOH-SRP, which is a small part (5%) of NaOH-TP), organic P (NaOH-NRP and refractory P), apatite P (HCl-TP), and dissolved pore water phosphorus from the decomposition of organic matter over time. Organic P is modeled as a portion of degradable organic matter, based on the Redfield stoichiometric composition. The modeling of the sorption capacity of phosphorus by the sediments was calculated using a modified Langmuir adsorption isotherm equation (Table 2 PBR1, Zhou et al., 2005), given in Table 3. Apatite P formation (Table 2, PBR2) is modeled using a precipitation dissociation reaction (Stumm and Morgan, 1996). The redox sensitive Fe–P fraction is modeled based on the assumption that Fe–P is formed in the presence of oxygen (Table 2, PBR3, Reed et al., 2011a) and will be reduced in the absence of  $O_2$  (Table 2, PBR4). The aluminum-bound fraction Al–P is modeled based on the Kopacek et al. (2005) laboratory experiments on the impact of Al on sediment sorption capacity.

2.2.3. Dataset and model parameters

Sediment and pore-water datasets collected from three study sites in the mesotrophic Lake Simcoe in March and September 2011 have been used to calibrate and validate the model, respectively (Dittrich et al., 2013). Samples were collected using a core sampler Uwitech in a 60 cm long sampling tube. Cores were obtained in March 2011 and September 2011 from three locations (C9, K42 and K45). Water depth profiles of dissolved oxygen, temperature, pH and conductivity were collected using a Seabird sensor at each sampling site before the sediment sampling occurred. The cores were sealed on site, to prevent any atmospheric exchanges, and were then transferred to the lab in a thermo-isolated custom built box, where they were preserved at 4 °C. Two cores were used for pore water analysis, and two to three cores were used for the fractionation of phosphorus, and the analysis of porosity, dry weight and total organic matter. Two to three sediment

**Table 2**  
Diagenetic reactions in the model.  $X_{org}$  indicates organic matter with the composition:  $C_{\alpha C/12}H_{\alpha H}O_{\alpha O/16}N_{\alpha N/14}P_{\alpha P/31}S_{\alpha S/32}$ . The stoichiometry coefficients of organic components are given in Table 4.

|   | Reactants                                 | Products   | Rates |
|---|---|--|-------|
| Primary redox reduction                     | $X_{org} + O_2 + H_2O$                    | $NH_4^+ + HPO_4^- + HCO_3^- + H^+ + HS^-$                  | PR1   |
|   | $X_{org} + NO_3^- + H_2O$                 | $NH_4^+ + HPO_4^- + HCO_3^- + H^+ + HS^- + N_2$            | PR2   |
|   | $X_{org} + X_{MnO_2} + H^+$               | $NH_4^+ + HPO_4^- + HCO_3^- + HS^- + H_2O + Mn^{2+}$       | PR3   |
|   | $X_{org} + X_{FeOOH} + H^+$               | $NH_4^+ + HPO_4^- + HCO_3^- + H^+ + HS^- + H_2O + Fe^{2+}$ | PR4   |
|   | $X_{org} + SO_4^{2-} + H_2O$              | $NH_4^+ + HPO_4^- + HCO_3^- + H^+ + HS^-$                  | PR5   |
| Secondary redox reaction                    | $NH_4^+ + 2O_2$                           | $NO_3^- + 2H^+ + H_2O$                                     | SR1   |
|   | $H_2S + 2O_2$                             | $SO_4^{2-} + 2H^+$   | SR2   |
|   | $8X_{FeOOH} + H_2S + 14H^+$               | $8Fe^{2+} + SO_4^{2-} + 12H_2O$                            | SR3   |
|   | $FeS + 2O_2$                              | $Fe^{2+} + SO_4^{2-}$                                      | SR4   |
| Mineral precipitation–dissolution reactions | $Mn^{2+} + HCO_3^-$                       | $X_{MnCO_3} + H^+$   | MR1   |
|   | $Ca^{2+} + HCO_3^-$                       | $X_{CaCO_3} + H^+$   | MR2   |
|   | $Fe^{2+} + CO_3^{2-}$                     | $2X_{FeCO_3}$  | MR3   |
|   | $Fe^{2+} + HS^-$                          | $X_{FeS} + H^+$  | MR4   |
| Acid base equilibrium conditions            | $H_2O$                                    | $H^+ + OH^-$   | ER1   |
|   | $H_2CO_3^*$                               | $HCO_3^- + H^+$  | ER2   |
|   | $HCO_3^-$                                 | $CO_3^{2-} + H^+$  | ER3   |
|   | $NH_4^+$                                  | $NH_3 + H^+$   | ER4   |
|   | $H_2PO_4^-$                               | $HPO_4^- + H^+$  | ER5   |
|   | $H_2S$                                    | $HS^- + H^+$   | ER6   |
|   | $HS^-$                                    | $S^{2-} + H^+$   | ER7   |
| Phosphorus binding forms reactions          | $HPO_4^-$                                 | $X_{Adsorbed\_P}$  | PBR1  |
|   | $3Ca^{2+} + 2HPO_4^{2-}$                  | $X_{Apatite\_P} + 4H^+$                                    | PBR2  |
|   | $4Fe^{2+} + 4HPO_4^{2-} + 8HCO_3^- + O_2$ | $4X_{Fe\_P} + 8CO_2 + 4X_{FeOOH}$                          | PBR3  |
|   | $X_{Fe\_P}$                               | $Fe^{2+} + HPO_4^-$  | PBR4  |
|   | $HPO_4^-$                                 | $X_{AL\_P}$  | PBR5  |

**Table 3**

Process rates of reactions in the model.  $S_i$  represents concentrations of a dissolved substance  $i$  and  $X_i$  indicates the concentration of the particulate substances  $i$ .

| Primary reduction  |   |  |
|--|---|--|
| $PR1 = k_{O_2} \frac{S_{O_2}}{K_{O_2} + S_{O_2}} X_{Org, fast}$  |   |  |
| $PR2 = k_{NO_3} \frac{K_{O_2}}{K_{O_2} + S_{O_2}} \frac{S_{NO_3}}{K_{NO_3} + S_{NO_3}} X_{Org, fast}$  |   |  |
| $PR3 = k_{MnO_2} \frac{K_{O_2}}{K_{O_2} + S_{O_2}} \frac{K_{NO_3}}{K_{NO_3} + S_{NO_3}} \frac{X_{MnO_2}}{K_{MnO_2} + X_{MnO_2}} X_{Org, fast}$   |   |  |
| $PR4 = k_{FeOOH} \frac{K_{O_2}}{K_{O_2} + S_{O_2}} \frac{K_{NO_3}}{K_{NO_3} + S_{NO_3}} \frac{K_{MnO_2}}{K_{MnO_2} + X_{MnO_2}} \frac{X_{FeOOH}}{K_{FeOOH} + X_{FeOOH}} X_{Org, fast}$   |   |  |
| $PR5 = k_{SO_4} \frac{K_{O_2}}{K_{O_2} + S_{O_2}} \frac{K_{NO_3}}{K_{NO_3} + S_{NO_3}} \frac{K_{MnO_2}}{K_{MnO_2} + X_{MnO_2}} \frac{X_{FeOOH}}{K_{FeOOH} + X_{FeOOH}} \frac{X_{SD4}}{K_{SD4} + X_{SD4}} X_{Org, fast}$  |   |  |
| Secondary reaction   |   |  |
| $SR1 = k_{nitri} \frac{S_{NH}}{k_{nitri, NH_4} + S_{NH_4}} \frac{S_O}{k_{nitri, O_2} + S_{O_2}}$   | $SR3 = k_{FeOOH} X_{FeOOH} S_{HS}$  |  |
| $SR2 = k_{oxi, HS} S_{HS} S_{O_2}$   | $SR4 = k_{FeSO} X_{FeS} S_{O_2}$  |  |
| Non-redox mineral precipitation–dissolution reactions  |   |  |
| $MR1 = \begin{cases} k_{eq, MnCO_3, prec} \left( \frac{S_{Mn} S_{CO_3}}{K_{eq, MnCO_3}} - 1 \right) & \text{if } \frac{S_{Mn} S_{CO_3}}{K_{eq, MnCO_3}} > 1 \\ k_{eq, MnCO_3, diss} \left( \frac{S_{Mn} S_{CO_3}}{K_{eq, MnCO_3}} - 1 \right) & \text{if } \frac{S_{Mn} S_{CO_3}}{K_{eq, MnCO_3}} < 1 \end{cases}$ | $MR3 = \begin{cases} k_{eq, FeCO_3, prec} \left( \frac{S_{Fe} S_{CO_3}}{K_{eq, FeCO_3}} - 1 \right) & \text{if } \frac{S_{Fe} S_{CO_3}}{K_{eq, FeCO_3}} > 1 \\ k_{eq, FeCO_3, diss} \left( \frac{S_{Fe} S_{CO_3}}{K_{eq, FeCO_3}} - 1 \right) X_{FeCO_3} & \text{if } \frac{S_{Fe} S_{CO_3}}{K_{eq, FeCO_3}} < 1 \end{cases}$ |  |
| $MR2 = \begin{cases} k_{eq, CaCO_3, prec} \left( \frac{S_{Ca} S_{CO_3}}{K_{eq, CaCO_3}} - 1 \right) & \text{if } \frac{S_{Ca} S_{CO_3}}{K_{eq, CaCO_3}} > 1 \\ k_{eq, CaCO_3, diss} \left( \frac{S_{Ca} S_{CO_3}}{K_{eq, CaCO_3}} - 1 \right) & \text{if } \frac{S_{Ca} S_{CO_3}}{K_{eq, CaCO_3}} < 1 \end{cases}$ | $MR4 = \begin{cases} k_{eq, FeS, prec} \left( \frac{S_{Fe} S_{S_2}}{K_{eq, FeS}} - 1 \right) & \text{if } \frac{S_{Fe} S_{S_2}}{K_{eq, FeS}} > 1 \\ k_{eq, FeS, diss} \left( \frac{S_{Fe} S_{S_2}}{K_{eq, FeS}} - 1 \right) X_{FeS} & \text{if } \frac{S_{Fe} S_{S_2}}{K_{eq, FeS}} < 1 \end{cases}$                          |  |
| Acid dissociation reactions  |   |  |
| $ER1 = k_{eq, w} \left( 1 - \frac{S_{H^+} S_{OH^-}}{K_{eq, w}} \right)$  | $ER4 = k_{eq, N} \left( S_{NH_4} - \frac{S_{H^+} S_{NH_3}}{K_{eq, N}} \right)$  | $ER6 = k_{eq, S_2} \left( S_{H_2S} - \frac{S_{H^+} S_{HS}}{K_{eq, S_1}} \right)$ |
| $ER2 = k_{eq, 1} \left( S_{CO_2} - \frac{S_{H^+} S_{HCO_3^-}}{K_{eq, 1}} \right)$  | $ER5 = k_{eq, P} \left( S_{H_2PO_4} - \frac{S_{H^+} S_{HPO_4^{2-}}}{K_{eq, P}} \right)$   | $ER7 = k_{eq, S_1} \left( S_{HS} - \frac{S_{H^+} S_{S_2}}{K_{eq, S_1}} \right)$  |
| $ER3 = k_{eq, 2} \left( S_{HCO_3^-} - \frac{S_{H^+} S_{CO_3^{2-}}}{K_{eq, 2}} \right)$   |   |  |
| Phosphorus binding form reactions  |   |  |
| $PBR1 = k_{Adsorb} \left( Q_{max} \frac{(K_{Adsorb, HPO_4} M_{HPO_4})}{(1 + (K_{Adsorb, HPO_4} M_{HPO_4}))} - X_{Adsorb, P} \right)$   | $PBR4 = k_{deg, BD} \frac{K_{O_2}}{K_{O_2} + S_{O_2}} X_{BD, P}$  |  |
| $PBR2 = \frac{\left( \frac{S_{Ca}}{1000} \right)^3 \left( \frac{S_{HPO_4}}{1000} \right)^2}{K_{eq, Apatite} + 10^{-4} pH}$   | $PBR5 = k_{AdsorbAl} \left( Q_{max, Al} \frac{(K_{Adsorb, Al, HPO_4} M_{HPO_4})}{(1 + (K_{Adsorb, Al, HPO_4} M_{HPO_4}))} - X_{Al, P} \right)$  |  |
| $PBR3 = k_{p\_BD} S_{O_2} S_{Fe}$  |   |  |

cores were sectioned in 1 to 2 cm thick slices. In most cases, the 0–1 cm, 1–2 cm, 2–4 cm, 4–6 cm and 6–10 cm horizons were pooled. For deep core analysis, the horizons 10–15 and 15–20 cm were also collected. The above-mentioned layers taken from the cores were added in a beaker and were then mixed. Samples from each layer, from the two to three cores, were combined and centrifuged (11,000 rpm × 10 min), decanted, and filtered (0.45 μm) for porewater analysis. Porewater depth profile data for Ca, Fe, Mn, NO<sub>3</sub>, HPO<sub>4</sub> as well as data on porosity, organic carbon and P fractions were measured in 2011. pH and O<sub>2</sub> profiles were measured with microsensors, while data on CaCO<sub>3</sub> were used from the Johnson and Nicholls (1989) study. More details on the experimental data have been published by Dittrich et al. (2013). Total Fe and Mn at the surface sediment and at the depth of ca. 24 cm have been measured by Landre et al. (2011). Data on alkalinity and ammonia at the SWI were assumed to be equal to the maximum deep water data measured by the 2004–2008 monitoring program (MOE, 2008).

The values of all model parameters are listed in Table 4 for the site K45. Equilibrium constants for acid–base equilibria were derived from Stumm and Morgan (1996). The equilibrium processes including Langmuir isotherms are formulated as dynamic processes with fast rate constants. The maximum rates of the degradation, dissolution, and precipitation processes were calibrated through the minimization of the sum of squares of the weighted deviations between observed data and model predictions. A number of specific parameters required for the model were derived from

the literature, such as sedimentation rates, bioturbation and sediment density (Johnson and Nicholls, 1989; MOE, 2010; Hiriart-Baer et al., 2011).

A previous study by Stantec (2006) provided estimates of benthic invertebrate abundance in the profundal zones of interest: ~2000 individuals/m<sup>2</sup> in station K42, 1600 individuals/m<sup>2</sup> in K45 and 17,200 individuals/m<sup>2</sup> in C9. The dominant species are suspension feeding chironomidae larvae (~50% for K45, ~36% for K42) which are burrow irrigators, deposit feeding oligochaetes (~43% for K42, 17% for C9) and dreissenid mussels (~16% for K45 and K42, ~46% for C9). The bivalve populations are represented by *Sphaeriidae*, which tend to burrow into the sediment substratum, and fingernail clams. Due to the complexity of the bivalve contribution to bioturbation and bioirrigation, the bivalve activity was lumped together with other species described above and uniform lakewide solute transport rates for bioturbation  $D_B = 30 \text{ cm}^2/\text{year}$  and bioirrigation  $\alpha = 10^{-7} \text{ s}^{-1}$  were assigned to parameterize their year-round activity; thus, the seasonal variability in the concentration of bottom dissolved oxygen or ice cover was not considered. In the absence of experimental measurements and information about the formation and dimensions of burrows, the <sup>22</sup>Na tracer diffusion rates were taken as a proxy for major solute variables of interest. We also introduced an exponential decay function for these rates to delimit the invertebrate's activity within the oxygenated zone in the sediments (Reed et al., 2011b). The bioirrigation term was accommodated with a non-local model (Boudreau, 1997; Couture and Van Cappellen, 2011).

**Table 4**

Parameters used in the sediment model for K45. \* indicates fitted parameter. DM indicates dry matter and OM indicates organic matter.

| Composition of organic components            | Atoms  | Mass fraction  |                        |
|--|--|--|------------------------|
| $\alpha_C$                                   | 106  | 0.358 g C/g OM   |                        |
| $\alpha_H$                                   | 263  | 0.074 g H/g OM   |                        |
| $\alpha_O$                                   | 110  | 0.496 g O/g OM   |                        |
| $\alpha_N$                                   | 16   | 0.063 g N/g OM   |                        |
| $\alpha_P$                                   | 1  | 0.009 g P/g OM   |                        |
| $\alpha_S$                                   | 0  | 0.000 g S/g OM   |                        |
| Total Redfield composition <sup>a</sup>      | 3550 <sup>a</sup>  | 1 g Tot/g OM   |                        |
| Symbol                                       | Description  | Value  | Units                  |
| <i>Proportional breakdown of total flux</i>  |  |  |                        |
| $\alpha_{Org}$                               | Fraction of OM   | 0.42   |                        |
| $\alpha_{Inorg}$                             | Fraction of inorganic matter                                     | $1 - \alpha_{Org}$   |                        |
| $\alpha_{Inorg\_P}$ *                        | Fraction of inorganic P  | $6.2e-6$   |                        |
| $\alpha_{Inorg\_P\_Fe-P}$ *                  | Fraction of redox-sensitive P                                    | 0.33   |                        |
| $\alpha_{Org\_inert}$ *                      | Fraction of refractory OM  | 0.52   |                        |
| $\alpha_{deg}$                               | Fraction of degradable OM  | $1 - \alpha_{Org\_inert}$  |                        |
| $\alpha_{Inorg\_Total\ Fe}$                  | Fraction of total settled iron                                   | $1 - (\alpha_{Inorg\_Other} + \alpha_{Inorg\_P})$                  |                        |
| $\alpha_{Inorg\_Fe\_FeOOH}$                  | Fraction of settled FeOOH  | $1 - \alpha_{Inorg\_Fe\_Other}$                                    |                        |
| $\alpha_{Inorg\_Fe\_Other}$                  | Fraction of settled inorganic Fe, excluding FeOOH                | 0.99   |                        |
| $\alpha_{Inorg\_P\_ApatiteP}$ *              | Fraction of settled apatite P                                    | $1 - \alpha_{Inorg\_P\_Fe-P}$                                      |                        |
| $\alpha_{Inorg\_Other}$                      | Fraction of inorganic matter without FeOOH and P                 | 0.9999   |                        |
| <i>Primary redox reactions</i>               |  |  |                        |
| $k_{O_2}$ *                                  | Rate constant of OM degradation with oxygen PR1                  | 0.024  | $d^{-1}$               |
| $k_{NO_3}$ *                                 | Rate constant of OM degradation with nitrate PR2                 | 2.09   | $d^{-1}$               |
| $k_{MnO_2}$ *                                | Rate constant of OM degradation with manganese oxides PR3        | $4.3e-6$   | $d^{-1}$               |
| $k_{FeOOH}$ *                                | Rate constant of OM degradation with iron hydroxides PR4         | $3.3e-7$   | $d^{-1}$               |
| $k_{SO_4}$ <sup>f</sup>                      | Rate constant of OM degradation with SO4 PR5                     | $1.0e-4$   | $d^{-1}$               |
| $K_{O_2}^{satur*}$                           | Half-saturation constant for OM degradation with oxygen          | 4.18   | mmol/l                 |
| $K_{NO_3}^{satur*}$                          | Half-saturation constant for OM degradation with nitrate         | 484.7  | mmol/l                 |
| $K_{MnO_2}^{satur*}$                         | Half-saturation constant for OM degradation with manganese oxide | 0.09   | mmol/g                 |
| $K_{FeOOH}^{satur*}$                         | Half-saturation constant for OM degradation with iron hydroxide  | 0.3  | mmol/g                 |
| $K_{SO_4}^{satur^f}$                         | Half-saturation constant for OM degradation with sulfate         | 0.005  | mmol/l                 |
| <i>Secondary redox reactions</i>             |  |  |                        |
| $k_{nitri}$ *                                | Rate constant for nitrification SR1                              | 0.37   | $d^{-1}$               |
| $K_{nitriNH_4}^{satur*}$                     | Half-saturation constant for nitrification                       | 1.9  | mmol/l                 |
| $k_{oxiHS}$                                  | Rate of secondary reaction SR2                                   | 0.001  | $l\ mmol^{-1}\ d^{-1}$ |
| $K_{oxiH_2S}^{satur*}$                       | Half-saturation constant for sulfide oxidation                   | 998.39   | mmol/l                 |
| $k_{FeOOHS}^g$                               | Rate of secondary reaction SR3                                   | 0.1  | $l\ mmol^{-1}\ d^{-1}$ |
| $k_{FeSO}^g$                                 | Rate of secondary reaction SR4                                   | 54.794   | $l\ mmol^{-1}\ d^{-1}$ |
| <i>Mineral dissolution and precipitation</i> |  |  |                        |
| $k_{eqMnCO_3prec}$                           | Rate constant for MnCO <sub>3</sub> precipitation, MR1           | $1.35e-5$  | mmol/l/d               |
| $K_{eqMnCO_3}^b$                             | Equilibrium constant for MnCO <sub>3</sub> , MR1                 | $10^{-10.4}$   | (mmol/l) <sup>2</sup>  |
| $k_{eqMnCO_3diss}$ *                         | Rate constant for MnCO <sub>3</sub> dissolution, MR1             | 0  | $d^{-1}$               |
| $k_{eqCaCO_3prec}$                           | Rate constant for CaCO <sub>3</sub> precipitation, MR2           | 0  | mmol/l/d               |
| $K_{eqCaCO_3}^b$                             | Equilibrium constant for CaCO <sub>3</sub> , MR2                 | $10^{(13.87 - 3059 / (273.15 + T) - 0.04035 * (273.15 + T))}$      | (mmol/l) <sup>2</sup>  |
| $k_{eqCaCO_3diss}$                           | Rate constant for CaCO <sub>3</sub> dissolution, MR2             | $2.5e-7$   | $d^{-1}$               |
| $k_{eqFeCO_3prec}$ *                         | Rate constant for FeCO <sub>3</sub> precipitation, MR3           | $1.35e-5$  | mol/l/d                |
| $K_{eqFeCO_3}^b$                             | Equilibrium constant for FeCO <sub>3</sub> , MR3                 | $10^{K_{eqFeCO_3num}}$   | (mmol/l) <sup>2</sup>  |
| $K_{eqFeCO_3num}^b$                          | See above  | -5   |                        |
| $k_{eqFeCO_3diss}$ *                         | Rate constant for FeCO <sub>3</sub> dissolution, MR3             | 0  | $d^{-1}$               |
| $k_{eqFeSprec}^f$                            | Rate constant for FeS precipitation, MR4                         | 0.002  | mmol/l/d               |
| $K_{eqFeS}^b$                                | Equilibrium constant for FeS, MR4                                | $10^{-12.1}$   | (mmol/l) <sup>2</sup>  |
| $k_{eqFeSdiss}^f$                            | Rate constant for FeS dissolution, MR4                           | 0  | $d^{-1}$               |
| <i>Acid base equilibrium conditions</i>      |  |  |                        |
| $k_{eqw}$ *                                  | Rate constant ER1  | 1000   | $d^{-1}$               |
| $K_{eqw}^b$                                  | Water dissociation constant                                      | $10^{(4470.99 / (273.15 + T) + 12.0875 - 0.01706 * (273.15 + T))}$ | (mmol/l) <sup>2</sup>  |
| $k_{eq1}$ *                                  | Rate constant ER2  | 1000   | $d^{-1}$               |
| $K_{eq1}^b$                                  | Dissociation constant ER2  | $10^{(14.843 - 3404.71 / (273.15 + T) - 0.032786 * (273.15 + T))}$ | (mmol/l) <sup>2</sup>  |
| $k_{eq2}$ *                                  | Rate constant ER3  | 1000   | $d^{-1}$               |
| $K_{eq2}^b$                                  | Dissociation constant ER3  | $10^{(6.494 - 2902.39 / (273.15 + T) - 0.02379 * (273.15 + T))}$   | (mmol/l) <sup>2</sup>  |
| $k_{eqN}$ *                                  | Equilibrium rate constant ER4                                    | 1000   | $d^{-1}$               |
| $K_{eqN}^c$                                  | Dissociation constant ER4  | $10^{(-0.09038 - 2729 / (273.15 + T))}$                            | (mmol/l) <sup>2</sup>  |
| $k_{eqP}$ *                                  | Equilibrium rate constant ER5                                    | 4.72   | $d^{-1}$               |
| $K_{eqP}^b$                                  | Dissociation constant ER5  | $10^{(-3.46 - 219.4 / (273.15 + T))}$                              | (mmol/l) <sup>2</sup>  |
| $k_{eqS1}$ *                                 | Equilibrium rate constant ER6                                    | 10,000   | $d^{-1}$               |
| $K_{eqS1}^b$                                 | Dissociation constant ER6  | $10^{(-0.14 - 1158 / (273.15 + T))}$                               | (mmol/l) <sup>2</sup>  |
| $k_{eqS2}$ *                                 | Equilibrium rate constant ER7                                    | 10,000   | $d^{-1}$               |
| $K_{eqS2}^b$                                 | Dissociation constant ER7  | $10^{(-2.03 - 2646 / (273.15 + T))}$                               | (mmol/l) <sup>2</sup>  |
| <i>P binding form reactions</i>              |  |  |                        |
| $K_{Adsorb}$                                 | Adsorption rate, PBR1  | 0.3  | $d^{-1}$               |
| $K_{Adsorb}^d$                               | Adsorption constant, PBR1  | 118.8  | l/mg                   |

(continued on next page)

Table 4 (continued)

| Symbol                               | Description   | Value       | Units                     |
|--------------------------------------|---|-------------|---------------------------|
| $Q_{\text{max}}^{\text{P}}$          | Maximal P adsorption sediment capacity, PBR1          | 12.7        | mg/g                      |
| $K_{\text{eq}}^{\text{Apatite}}$     | Dissociation constant PBR2                            | $10^{18.4}$ | $(\text{mmol/l})^2$       |
| $k_{\text{Fe-P}}^*$                  | Rate constant for Fe–P formation, PBR3                | $1.5e-4$    | $(\text{mM d})^{-1}$      |
| $k_{\text{degFe-P}}^*$               | Rate constant for Fe–P degradation PBR4               | $8.6e-6$    | $\text{d}^{-1}$           |
| $k_{\text{Adsorb-Al}}^*$             | Adsorption rate for Al–P, PBR5                        | 0.3         | $\text{d}^{-1}$           |
| $K_{\text{Adsorb-Al}}^{\text{d}}$    | Adsorption constant for Al–P, PBR5                    | 1.0         | l/mg                      |
| $Q_{\text{max-Al}}^{\text{h}}$       | Maximal P adsorption sediment capacity for Al–P, PBR5 | 0.46        | mg/g                      |
| <b>Compaction</b>                    |   |             |                           |
| $\theta_{\text{surf}}$               | Porosity at the SWI                                   | 0.91        |                           |
| $\theta_{\text{deep}}$               | Porosity at 19.5 cm (core bottom)                     | 0.8         |                           |
| $k_{\theta}^*$                       | Rate of porosity compaction                           | $7e-5$      | $\text{d}^{-1}$           |
| <b>Boundary conditions</b>           |   |             |                           |
| <b>Concentrations at the SWI</b>     |   |             |                           |
| $S_{\text{O}_2}^{\text{high SWI}}$   | Oxygen during mixed period                            | 0.30        | mmol/l                    |
| $S_{\text{O}_2}^{\text{low SWI}}$    | Oxygen during summer stratified period                | 0.13        | mmol/l                    |
| $S_{\text{NO}_3}^{\text{SWI}}$       | Nitrate, annual average                               | 0.022       | mmol/l                    |
| $S_{\text{NH}_4}^{\text{mean SWI}}$  | Ammonium, annual average                              | 0.05        | mmol/l                    |
| $S_{\text{HPO}_4}^{\text{mean SWI}}$ | Dissolved phosphorus, annual average                  | $7.9e-8$    | mmol/l                    |
| $S_{\text{Mn}}^{\text{SWI}}$         | Dissolved manganese                                   | 0.017       | mmol/l                    |
| $S_{\text{Fe}}^{\text{SWI}}$         | Dissolved iron  | 0.008       | mmol/l                    |
| $S_{\text{SO}_4}^{\text{SWI}}$       | Sulfate   | 0.03        | mmol/l                    |
| $S_{\text{Ca}}^{\text{SWI}}$         | Dissolved calcium                                     | 1.03        | mmol/l                    |
| $S_{\text{H}}^{\text{SWI}}$          | Hydrogen ions   | $6.76e-5$   | mmol/l                    |
| $S_{\text{HCO}_3}^{\text{SWI}}$      | Bicarbonate, $\text{HCO}_3^-$                         | 3.63        | mmol/l                    |
| $S_{\text{HS}}^{\text{SWI}}$         | Hydrogen sulfide, HS                                  | 0.00        | mmol/l                    |
| $S_{\text{S}_2}^{\text{SWI}}$        | Sulfide $\text{S}^{2-}$                               | $2.3e-10$   | mmol/l                    |
| <b>Fluxes at the SWI</b>             |   |             |                           |
| $f_{\text{org,mean}}$                | Organic matter, annual average                        | 0.32        | $\text{gDM/m}^2/\text{d}$ |
| $f_{\text{org,amplitude}}$           | Organic matter, amplitude                             | 0.08        | $\text{gDM/m}^2/\text{d}$ |
| $f_{\text{inorg}}$                   | Inorganic matter                                      | 0.44        | $\text{gDM/m}^2/\text{d}$ |
| $f_{\text{MnO}_2}^{\text{mean}}$     | Manganese oxide, annual average                       | $1.8e-5$    | $\text{mol/m}^2/\text{d}$ |
| $f_{\text{FeOOH}}^{\text{mean}}$     | Iron hydroxide, annual average                        | $4.13e-7$   | $\text{mol/m}^2/\text{d}$ |
| $f_{\text{CaCO}_3}^{\text{mean}}$    | Calcium carbonate, annual average                     | $2.5e-3$    | $\text{mol/m}^2/\text{d}$ |
| $f_{\text{FeS}}$                     | Iron sulfide  | $9.0e-7$    | $\text{mol/m}^2/\text{d}$ |
| $f_{\text{ApatiteP}}$                | Apatite P   | $1.8e-6$    | $\text{mol/m}^2/\text{d}$ |
| $f_{\text{Fe-P}}$                    | Iron-bound P  | $9.0e-7$    | $\text{mol/m}^2/\text{d}$ |
| $f_{\text{Al-P}}$                    | Aluminum bound P                                      | $9.0e-7$    | $\text{mol/m}^2/\text{d}$ |

<sup>a</sup> Klausmeier et al. (2004).

<sup>b</sup> Stumm and Morgan (1996).

<sup>c</sup> Clegg and Whitfield (1995).

<sup>d</sup> Dong et al. (2011).

<sup>e</sup> Reed et al. (2011b).

<sup>f</sup> Dittrich et al. (2009).

<sup>g</sup> Katsev et al. (2006).

<sup>h</sup> Kopacek et al. (2005).

## 2.2.4. Boundary conditions

**2.2.4.1. Solid components.** The boundary conditions for the sedimentation fluxes are defined with a piece-wise approach, postulating that the maximum flux of particulate matter occurs in summer and the minimum in winter (Fig. 4). The organic and inorganic components of the total flux are shown in Fig. 3, and the proportion of each component was determined through the model calibration. The beginning of the simulations for each sampling station was determined using sedimentation rates taken from Landre et al. (2011). The starting dates reflected the sediment depth determined as 1760 AD, 1607 AD and 1432 AD for stations C9, K42 and K45, respectively. The fluxes of FeS and  $\text{Fe}_3\text{PO}_4$  were set equal to zero at the sediment–water interface.

**2.2.4.2. Dissolved components.** The boundary conditions for the  $\text{O}_2$  concentrations at the SWI were also defined with a piece-wise approach, postulating that the maximum  $\text{O}_2$  concentration occurs in the winter, when there is less consumption from the biota, and the minimum concentration in the summer, when the lake is stratified (Fig. 4). The boundary conditions are given in Table 4. Finally, the temperature in the sediment was treated as a constant throughout the sediment depth profile, according to the empirical patterns reported in Lake Simcoe.

## 2.3. Sensitivity and identifiability analysis

Our sensitivity and identifiability analysis follows the framework originally introduced by Brun et al. (2001), which is founded upon the derivation of linear sensitivity functions for each state variable  $y_i$  against any parameter  $\theta_j$ :

$$s_{ij} = \frac{\Delta\theta_j \partial y_i}{s_{c_i} \partial \theta_j} \quad (7)$$

where  $\Delta\theta_j$  represents an a priori uncertainty range of the parameter  $\theta_j$ , set equal to 10%, and  $s_{c_i}$  is a scale factor of the state variable  $y_i$ . The factors  $s_{c_i}$  are used to scale the model outputs and thus make the results for the various model endpoints comparable. In this study, the scale factors were set equal to the maximum concentrations of each substance and are listed in Table 1 of the Supplementary Material. The parameter sensitivity ranking was subsequently based on the following sensitivity measure:

$$\delta_j = \sqrt{\frac{1}{n} \sum_{i=1}^n s_{ij}^2} = \frac{1}{\sqrt{n}} \|s_j\| \quad (8)$$

where  $\|s_j\|$  represents the norm of the vector of  $s_j$  which depicts the importance of the parameter  $\theta_j$ . A large norm implies that a perturbation

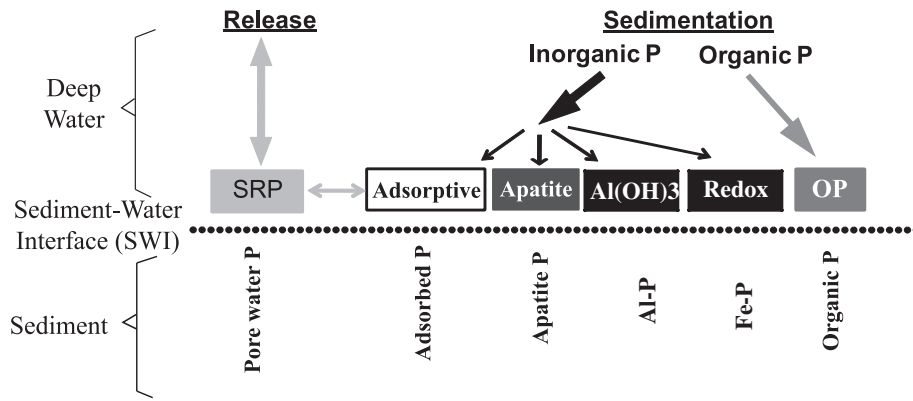


Fig. 2. Conceptual diagram of the presented phosphorus fractionation model in Lake Simcoe.

in a particular parameter induces significant changes on the vector of the  $n$  model endpoints, which in turn makes the parameter identifiable given the available data, if all other parameters remain fixed.

In a general context though, we can state that a set of model parameters  $\theta$  is identifiable from the calibration data, only if the following criteria are simultaneously met:

1. Model outputs  $y_i$  should indicate sensitive dependence on the parameter set  $\theta$ . With an increasing number of parameters, model sensitivity is expected to decrease.
2. A change in model outputs  $y_i$  caused by a relative change in one parameter  $\theta_j$  should not be compensated by a change in other parameters of the same set  $\theta$ .

The information on the sensitivity of model outputs on parameters can be combined with information on the degree of linear dependence (or collinearity) of sensitivity functions in order to find parameter sets that can be estimated from experimental/field data (Omlin et al., 2001). The analysis of the degree of linear dependence of sensitivity functions is similar to the technique recommended for collinearity analysis of influence factors in linear regression (Belsley et al., 1980; Belsley, 1991; Draper and Smith, 1998). If the sensitivity functions  $s_{ij}$  for a given parameter set are linearly dependent, changes in model outputs induced by a small change in one parameter can be approximately compensated by appropriate changes in other parameters of the same parameter set.

In this study, we have applied the identifiability framework proposed by Brun et al. (2001), using the collinearity index  $\gamma$  to assess the degree of near-linear dependence among  $k$  parameters in a particular subset.

$$\gamma_k = \frac{1}{\min_{\|\beta\|=1} \|\hat{S}\beta\|} \quad (9)$$

where  $\hat{S} = \begin{bmatrix} \hat{S}_{11} & \dots & \hat{S}_{1k} \\ \dots & \dots & \dots \\ \hat{S}_{n1} & \dots & \hat{S}_{nk} \end{bmatrix}$  represents the matrix of the normalized sensitivities of the  $k$  parameters in the subset, i.e.,  $\hat{S}_{ik} = \frac{s_{ik}}{\|s_k\|}$ , against the  $n$  model outputs, and  $\beta = (\beta_1, \dots, \beta_k)^T$  represents a vector of coefficients with the constraint  $\|\beta\| = 1$ . In essence, the  $\gamma$  index measures linear dependence among a subset of parameters as the reciprocal of the minimum norm that can be obtained by the linear combination  $\hat{S}\beta$ , which in turn is known to be equal to the square root of the smallest eigenvalue of the matrix  $\hat{S}^T\hat{S}$  (Beisley, 1991). A  $\gamma$  value equal to 1 suggests absence of collinearity, whereas a value of 20 suggests that a change in the model outputs caused by a shift in a parameter  $\theta_j$  can be compensated to 5% by appropriate adjustments in the other parameters of the subset. A high value of a collinearity index thus indicates that the parameter set is poorly identifiable, even if the individual parameters are very influential to the model output. In particular, any  $\gamma$  value higher than 10 depicts a relatively serious identifiability problem (Brun et al., 2001).

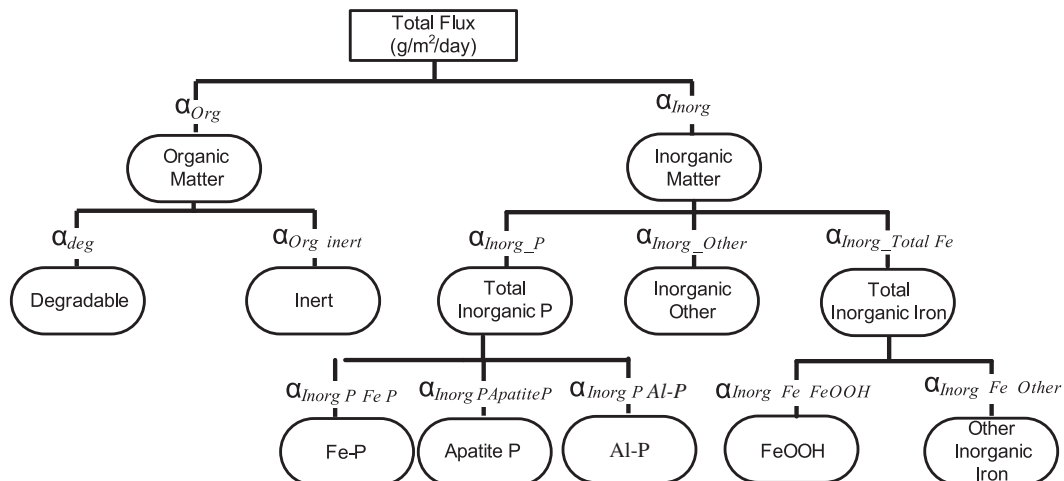


Fig. 3. Schematic diagram for the breakdown of the incoming flux of settling matter.

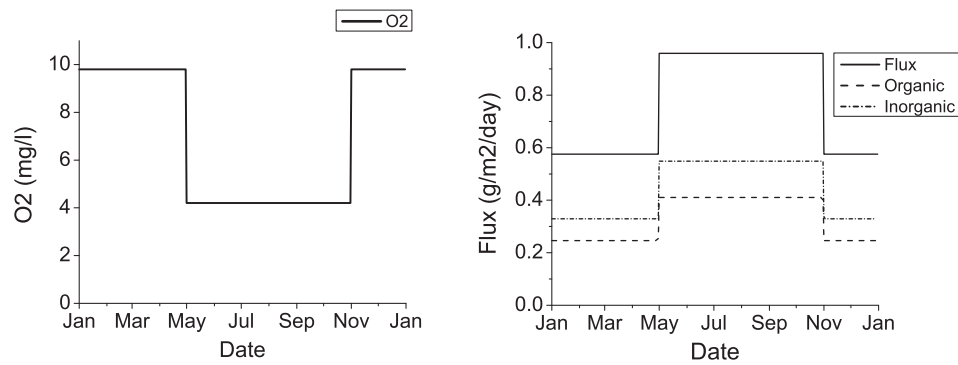


Fig. 4. Boundary conditions for sedimentation flux and initial oxygen concentrations over a one year time period. Sedimentation flux of total matter ( $\text{g}/\text{m}^2/\text{day}$ ), solid gray line, and initial  $\text{O}_2$  concentration,  $\text{mg}/\text{l}$ , dashed black line, are shown for the site K45 in the year 2005.

### 2.3.1. Numerical implementation

The model equations were implemented in the computer program AQUASIM (Reichert, 1994; Reichert, 1995; <http://www.aquasim.eawag.ch>), designed for simulation and data analysis of aquatic systems.

This program first discretizes the spatial derivatives of the partial differential equations and then integrates the resulting system of ordinary differential equations in time with the DASSL implementation (Petzold, 1983) of the implicit (backward differencing) variable-step, variable-

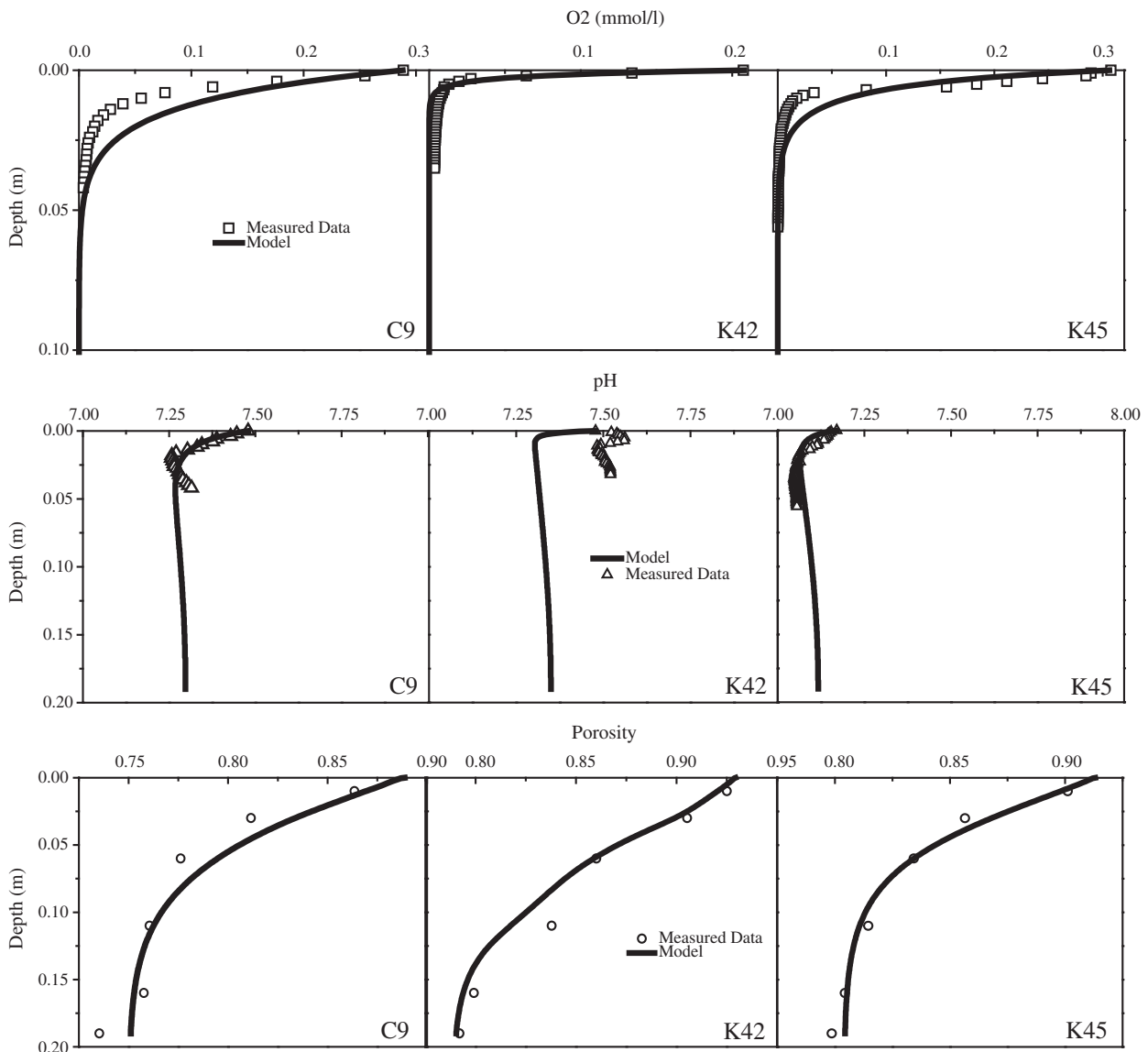
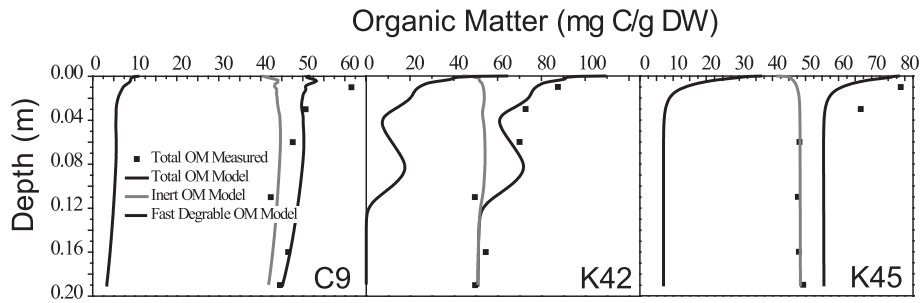


Fig. 5. Modeled and measured depth profiles of pH from site C9 (left),  $\text{O}_2$  from site K42 (center) and porosity from site K45 (right). Measured data are depicted by open squares and model output is given by a solid black line for each site.



**Fig. 6.** Modeled organic matter sediment profiles for 3 sites. Measured data are represented by symbols, square for total OM, and circle for inert OM. Model is represented by lines, total OM by solid black line, fast degradable OM by black dashed line, and inert OM by gray dashed line.

order GEAR integration technique (Gear, 1971). The sediment depth profile of 19 cm was discretized with 250 grid space planes. The identifiability analysis was performed with the IDENT package (<http://www.aquasim.eawag.ch>). The model has been calibrated for the data set collected from three stations (K45, K42 and C9) in March 2011 and validated against the data collected in September 2011. Sensitivity and identifiability analysis presented below has been performed for station K45, as a representative site for the whole lake.

**3. Results**

**3.1. Depth profiles of solids and dissolved substances**

The modeled outputs for the porosity and pH of the sediments are shown in Fig. 5. Our results suggest that the model accurately reproduces porosity, and also provides a good representation of the sediment pH in sites K45 and C9 but underestimates pH in K42. Because pH is a sensitive integrating indicator for a set of biogeochemical reactions (Jourabchi et al., 2005), the good agreement between the modeled and measured values of pH for sites K45 and C9 indicates that the simulated reaction/processes were generally plausible. The model also reproduced the fact that each site differs in regard to its oxygen profile (Fig. 5). Site K42 has a very shallow penetration depth of 1 cm, while C9 has a deeper penetration depth of 2.5 cm and K45 falls in the middle around 2 cm. The oxygen penetration depths reflect the oxygen demand for the mineralization of the settling organic matter, and are closely associated with the boundary conditions assigned to each site. In Kempenfelt Bay (K42), the sedimentation flux has a very high portion of organic matter (Fig. 4), which underscores the elevated primary production rates in the water column. By contrast, the sedimentation fluxes in C9 and K45 have much lower proportions of organic matter and thus higher O<sub>2</sub> penetration depths. Furthermore, the model reproduced the depth profiles of solid matter with good accuracy (Fig. 6). Each site shows a decrease of organic matter from the sediment surface to about 10 cm and remains relatively constant below that point. The difference between the surface

concentration, ~80–90 mg C/g DM for K45 and K42 and ~60 mg C/g DM for C9, and the deeper stabilized concentration (at approximately 10 cm depth) is the amount of organic matter mineralized in the sediment.

The model calibration was carried out with the boundary conditions described above, and aimed at reproducing the general trends observed in the pore water and solid sediment depth profiles. Initial values of the reaction parameters were taken from our previous experimental study (Dittrich et al., 2009) as well as from the literature, and their values were further adjusted to fit the experimental data while taking into account the parameter ranges reported in the literature (Table 3). We also conducted a model validation exercise, which showed good agreement between empirical and simulated depth profiles for solute and solid matter for September 2010, rendering support to the model parameterization.

**3.2. Depth profiles of phosphorus in sediments**

The model successfully reproduced the P fractionation data, i.e., adsorbed P, organic P, apatite P, Al-P and redox sensitive (Fe-P), as well as the total phosphorus at each site (Fig. 7). However, at site C9, the calculated fraction of adsorbed P is lower than those measured, indicative of the fact that this site is dominated by sediment erosion from the surrounding intensive agricultural areas. Most likely other geochemical (e.g. including nitrogen) and transport processes are crucial for the P-adsorption to the sediments at this basin. The organic P fraction and the total phosphorus (TP) closely resemble the total organic matter profiles, as they are high at the surface and then level out in the deeper sediments. The difference between the surface concentration and the deeper layers represents the P release from the sediments. At sites K45 and C9, the organic P fraction is responsible for most of the P release. The model predicts that most of the dissolved P is released into the overlying water column and that only a small fraction of the deposited reactive Fe is ultimately buried as FeS(s) (Fig. 7). Interestingly, site K42 shows a large amount of redox sensitive P at the surface as well as a large amount of organic P (Fig. 7), implying that a much

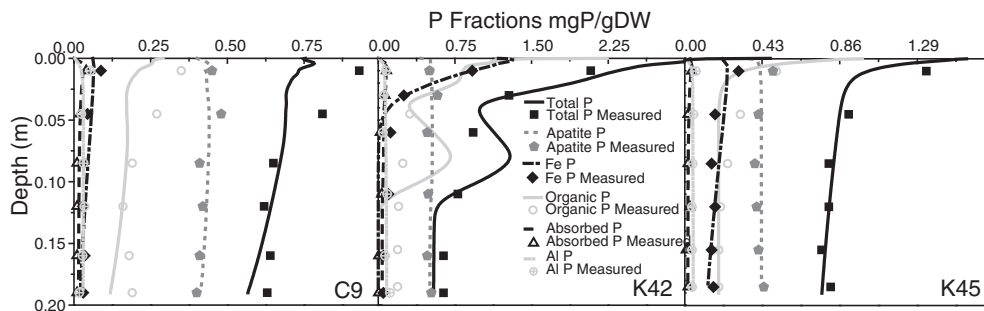


**Fig. 7.** Total phosphorus and P fraction profiles for 3 sites. Measured data are represented by symbols, square for total P, circle for organic P, triangle for adsorbed P, diamond for redox sensitive P, and pentagon for apatite P. Model is represented by lines, total P by solid black line, apatite P by solid gray line, adsorbed P by light gray dashed line, organic P by gray dashed line, and redox sensitive P by dark gray dash dot line.

greater P flux from the sediments to the water column should be expected if conditions at the sediment–water interface become anoxic. A constant amount of apatite and adsorbed P in the fractionation profiles is indicative of their immobilization in the sediments. For each site, apatite P is the predominant fraction suggesting a large P retention capacity in Lake Simcoe sediments (Fig. 7).

The modeled dissolved phosphorus profiles provide a reasonable description of the phosphate concentration gradient at the sediment–water interface (Fig. 8), despite the challenges posed by the substantial spatial and temporal variability in Lake Simcoe (Lewandowski et al., 2002). The latter pattern also suggests significant seasonality of the internal P release. Based on Fick's Law, the estimated benthic fluxes vary seasonally from 0.05 to 0.3 mg P/m<sup>2</sup>/d, which is similar to the estimate derived from measured P profiles (Dittrich et al., 2013). According to our model results, Kempenfelt Bay (K42) exhibits the highest gradient in depth profile of dissolved phosphorus, primarily driven by the release of the redox sensitive P fraction along with the higher degradation kinetics that deplete oxygen after the top 3–4 cm of sediments. This finding is also on par with the empirical evidence that Kempenfelt Bay was experiencing hypoxia problems and internal P loading (Evans, 2007; Nürnberg et al., 2013).

#### 4. Discussion: seasonal versus long-term dynamics of P binding forms at the sediment surface

The model results demonstrate strong seasonal dynamics of P-binding forms (Fig. 9), and their trends are closely linked to organic matter fluxes and oxygen concentrations at the sediment–water interface (see Table 5). In particular, it has been argued that P dynamics in Lake Simcoe, a “marl lake”, may be connected to whiting events or CaCO<sub>3</sub> precipitation in the water column during summer stratification (Nicholls, 1995). In many hard-water lakes, P is supposed to co-precipitate with calcium carbonates formed in the water column (Koschel et al., 1983; House, 1990). Our results provide evidence in support of this hypothesis as both organic P and apatite P are located in the surface sediments during the summer stratification (Fig. 9). This pattern has been observed in other hard-water lakes during artificial deep water (Dittrich et al., 2011) or natural (Gonsiorczyk et al., 1998) calcium carbonate precipitation. The whiting phenomenon is an important characteristic for the ecological health and self-recovery of hard-water lakes (Koschel et al., 1983), and has been applied as ecological technology for lake restorations (Dittrich et al., 2011). Consequently, the dynamic simulation of sediment diagenesis can conceivably support decision makers by providing projections of the long-term sediment response when a possible treatment is implemented (Schäuser et al., 2003).

In all basins, the low flux of organic matter in winter coincides with the peak oxygen and low organic P concentrations. Likewise, diagenesis models for marine systems found a strong link between hypoxia and P forms in sediments in the Baltic Sea (Reed et al., 2011b). Model simulations showed that the variability of redox-sensitive P is driven by total sedimentation flux dynamics and oxygen concentration at the

sediment–water interface. According to data from sediment mapping (Landre et al., 2011), iron is enriched in all sediment layers in Kempenfelt Bay and therefore is readily available as a P binding partner. On the other hand, if conditions at the sediment surface become anoxic, dissolution of iron hydroxides will be intensified leading to the release of redox sensitive P.

Despite being the smallest fraction in absolute values, the adsorbed P-fraction demonstrated significant variability, which was captured by the model. This finding is very promising from a management perspective. The adsorbed-P fraction is in equilibrium with P in the porewater, thereby determining the diffusive flux into the water column. Thus, our model can provide decision makers with a reliable prediction of diffusive P flux from the sediments into water column and contribute to the estimation of internal loading (Fig. 11), which is a controversial issue for mesotrophic lakes as well as lakes in a transitional phase (Nürnberg, 1988; Rydin, 2000; Katsev et al., 2006). Our model predicts that the Al-P fraction exhibits seasonal variability. Being a redox insensitive fraction, Al-P is important for P immobilization (Kopacek et al., 2005). Naturally high (or artificially elevated) concentrations of aluminum hydroxide (Al(OH)<sub>3</sub>) have been shown to naturally lower (or artificially reduce) hypolimnetic P release that typically occurs under reducing conditions. The molar ratios of Al-P to Fe-P can be operationally used as targets for estimating the potential sediment P release and Al dosing of P-rich sediments to prevent hypolimnetic P release under anoxic conditions (Kopacek et al., 2005). The presented model allows estimation of this ratio and subsequent prediction of its broader implications in the system dynamics. Therefore, it is of wide interest for investigations of both natural and artificially treated sediments under reducing conditions.

However, it is also the second smallest fraction in absolute values (ca. 1% of TP), and thus cannot determine the extent of P immobilization. The molar ratio between Al in Al-P fraction to Fe in Fe-P fraction is around 2.7, which is close to the threshold value for redox sensitive P release from sediments (Kopacek et al., 2005). This ratio has been used as an operational target for preventing hypolimnetic P release under anoxic conditions, and when it is greater than 3, P release under reducing conditions practically ceases (Kopacek et al., 2005).

Quite recently, a detailed paleo-limnological study documented sedimentation rates for three basins of Lake Simcoe (Hiriart-Baer et al., 2011). Using this data, we simulated the P binding forms at the sediment surface through a 400-yr period (Fig. 10 upper panel). The modeled long-term patterns of P-fraction reflect a complex interplay between the total sedimentation fluxes and P transformations (Fig. 10, Table 2). In Cook's Bay (C9), the two-fold increase in the total loading after the 1940s resulted in an accumulation of apatite P in the surface sediments. Apatite P includes phosphorus incorporated in carbonates, formed by both autochthonous (e.g., P co-precipitated with carbonates during whiting events, Gonsiorczyk et al., 1998) or allochthonous (e.g., phosphorus in soil particles flushed from the catchment) material. Thus, the increase of apatite P may reflect both an increase of CaCO<sub>3</sub> precipitation within the lake and/or increased erosion from the catchment. In the case of Cook's Bay, the documented history of land use provides

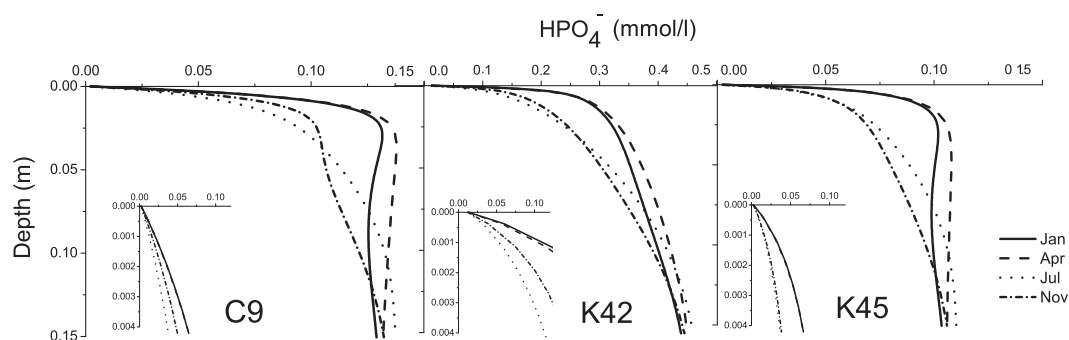
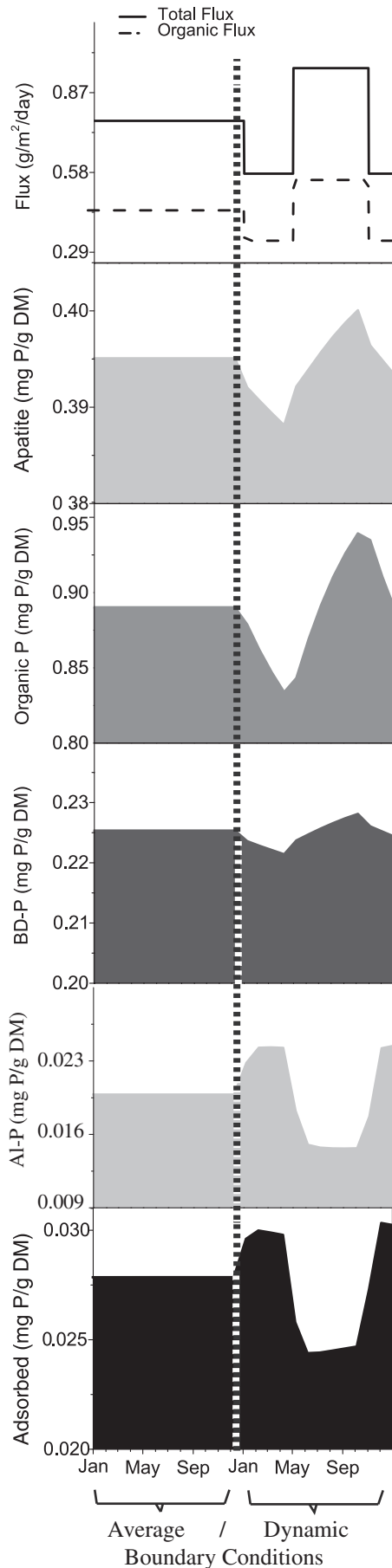


Fig. 8. Modeled dynamics of dissolved phosphorus ( $\text{HPO}_4^-$ ) in three basins of Lake Simcoe in 2011.



**Table 5**

Ranking of relative sensitivities of model with respect to 37 model parameters. The parameters  $k$  are process rate constants. Those with index “eq” are equilibrium dissociation, precipitation or dissolution rate constant. The parameters  $K^{sat}$  are half-saturation concentrations of degradation processes. The parameters  $S^{SWI}$  are concentrations of dissolved substances at the sediment–water interface. The parameters  $f$  are mass fluxes of sedimenting particles. Sensitivity rankings are based on diagenesis model at Main Basin, K45.

| Rank | Name                        | $\delta^{msqr}$ |
|------|-----------------------------|-----------------|
| 1    | $S_{O_2}^{SWI}$             | 31.9            |
| 2    | $S_H^{SWI}$                 | 20.6            |
| 3    | $\alpha_{Org}$              | 4.9             |
| 4    | $\alpha_{Org\_inert}$       | 4.8             |
| 5    | $S_{HCO_3}^{SWI}$           | 4.1             |
| 6    | $S_{NO_3}^{SWI}$            | 3.7             |
| 7    | $\alpha_{Inorg\_P\_Fe-P}$   | 3.5             |
| 8    | $D_B$                       | 2.5             |
| 9    | $k_{degFe-P}$               | 2.3             |
| 10   | $K_{eq,FeCO_3}$             | 2.3             |
| 11   | $k_{O_2}$                   | 1.5             |
| 12   | $K^{sat}_{O_2}$             | 1.3             |
| 13   | $f_{CaCO_3}$                | 1.3             |
| 14   | $Q_{max}$                   | 1.3             |
| 15   | $\alpha_{Inorg\_Fe\_Other}$ | 1.0             |
| 16   | $k_{eq,CaCO_3,diss}$        | 1.0             |
| 17   | $\alpha_{bioirrig}$         | 1.0             |
| 18   | $k_\theta$                  | 0.6             |
| 19   | $k_{nitri}$                 | 0.51            |
| 20   | $S_{Ca}^{SWI}$              | 0.47            |
| 21   | $k_{oxi, HS}$               | 0.32            |
| 22   | $k_{MnO_2}$                 | 0.30            |
| 23   | $S_{Fe}^{SWI}$              | 0.28            |
| 24   | $K_{Adsorb}$                | 0.26            |
| 25   | $K_{FeOOH}$                 | 0.25            |
| 26   | $k_{NO_3}$                  | 0.20            |
| 27   | $S_{Mn}^{SWI}$              | 0.18            |
| 28   | $S_{HS}^{SWI}$              | 0.17            |
| 29   | $K_{NO_3}$                  | 0.16            |
| 30   | $k_{FeOOH}$                 | 0.16            |
| 31   | $K_{eq,Apatite}$            | 0.11            |
| 32   | $f_{MnO_2}$                 | 0.071           |
| 33   | $K_{MnO_2}$                 | 0.064           |
| 34   | $k_{Fe-P}$                  | 0.047           |

evidence that apatite P accumulation has likely occurred due to an increase of the agricultural activities and subsequently erosion (Hiriart-Baer et al., 2011).

By contrast, the sediments in Kempenfelt Bay (K42) accumulated organic-P (Fig. 10, middle column). This accumulation is particularly pronounced after the 1940s, coinciding with the expansion of urbanization and other associated anthropogenic activities (LSRCA, 1993). This finding is also in agreement with a recent  $^{13}C$  isotope analysis, asserting that wastewater effluent might be a dominant driver of P-loading in Kempenfelt basin (Hiriart-Baer et al., 2011). The high amount of redox sensitive P supports the empirical evidence that this basin has experienced severe hypoxia events from the 1980s until the mid 1990s. The high Fe amount due to the geological background of Kempenfelt Bay provides a redox-dependent binding capacity for phosphorus on iron oxides and hydroxides. However, under reducing conditions induced by hypoxia, redox-bounded P can be dissolved (Reed et al., 2011b), and this pattern has often been observed in various stratified freshwater systems (e.g., Hupfer et al., 1995; Ulrich, 1997).

4.1. Which processes impact the dynamics of P binding forms in the sediments?

Sensitivity analysis allows us to determine the subset of parameters that are most influential on model predictions (Brun et al., 2001; Omlin

**Fig. 9.** Impact of dynamics of sedimentation flux on P binding forms in surface sediments for site K45 in 2004 and 2005. Values for P binding forms are an average of the top 6 mm of the sediments.

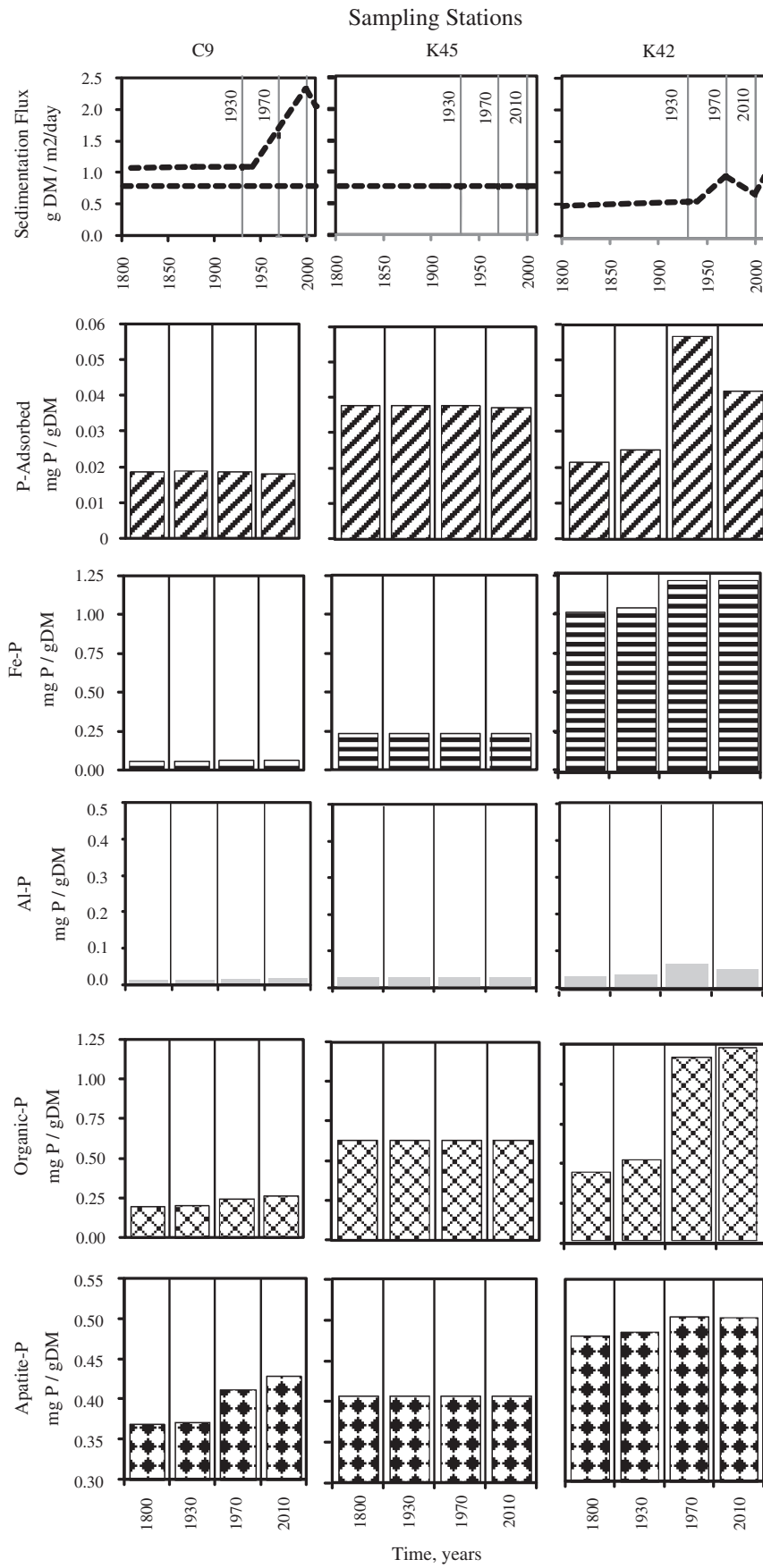


Fig. 10. Impact of long-term dynamics of sedimentation flux on P binding forms in surface sediments.

et al., 2001; Arhonditsis and Brett, 2004; Katsev et al., 2006). Sensitivity analysis can dictate which parameters need to be constrained with more information from the field and/or the literature. Our sensitivity analysis has been carried out for the main basin, as this station is the most representative for the whole-lake P retention in the sediments. The ranking of the 34 parameters considered has been calculated using the sensitivity measure  $\delta$  (Table 5). The central conclusion drawn from our study is that in order to elucidate the P diagenesis processes and subsequently predict P efflux to the water column of a hard-water mesotrophic lake, the concentrations of dissolved substances such as oxygen ( $S_{O_2}^{SWI}$ ), pH ( $S_H^{SWI}$ ), alkalinity ( $S_{HCO_3}^{SWI}$ ), nitrate ( $S_{NO_3}^{SWI}$ ), calcium ( $S_{Ca}^{SWI}$ ), iron ( $S_{Fe}^{SWI}$ ), manganese ( $S_{Mn}^{SWI}$ ), and the sedimentation fluxes of organic and inorganic matter ( $\alpha_{Org}$ ,  $\alpha_{Org\_inert}$ ) should be accurately determined in addition to P species.

#### 4.2. Oxygen and pH at the sediment–water interface and composition of settling matter

Our results primarily highlight the sensitivity of the modeled outputs to  $S_{O_2}^{SWI}$  and pH ( $S_H^{SWI}$ ). The model is also sensitive to the composition of settling matter; especially, the portions of organic reactive and refractory carbon ( $\alpha_{Org}$  and  $\alpha_{Org\_inert}$ ). The second group of parameters comprises alkalinity ( $S_{HCO_3}^{SWI}$ ), nitrate concentrations ( $S_{NO_3}^{SWI}$ ), the settling part of redox sensitive phosphorus ( $\alpha_{Inorg\_P\_Fe-P}$ ), bioturbation ( $D_{Bioturbation}$ ), the degradation rate of redox sensitive phosphorus ( $k_{degFe-P}$ ) and the equilibrium constant of siderite ( $K_{eq,FeCO_3,num}$ ). Interestingly, bioturbation appears to be a critical factor in the model, even though the effect of benthic invertebrates is only limited to the oxygenated layer. Thus, it is necessary to have experimental evidence for the functional role of benthic organisms in stratified mesotrophic lakes, if one wants to understand phosphorus diagenesis over time. Chironomids can potentially increase the flux of dissolved phosphorus from the sediments by ingesting large quantities of interstitial pore water, while the combined effect of bioturbation and bioirrigation is insignificant under anoxic conditions (Graneli, 1999). The small-scale movements of bivalves aside from their bio-diffusing activity can potentially induce a bioturbation effect on the sediments, if they are able to bury into the sediment bed, and thus increase the nutrient flux. Depending on their abundance, bivalves can also become an additional source of organic matter as well as a sink of dissolved oxygen through their respiration. In the next iteration of the model, our aim is to explicitly consider the seasonality of benthic activity, thereby leading to a more realistic simulation of their role in P retention.

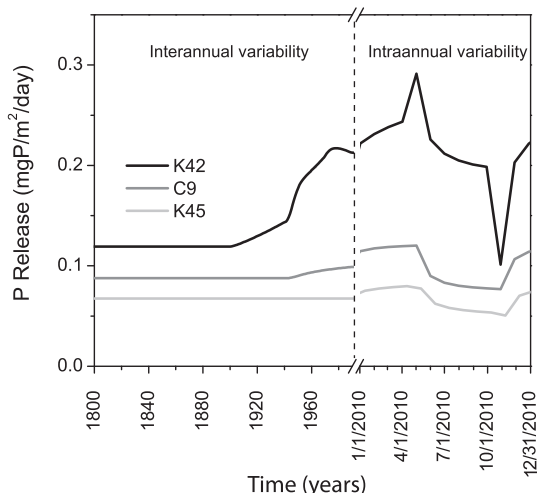


Fig. 11. Modeled dissolved phosphorus release rates for 3 sites.

#### 4.3. Sedimentation of calcium carbonates and P adsorption/binding to carbonates

A lower sensitivity index has been found for the two parameters representing the role of oxygen with the degradation processes ( $k_{O_2}$  and  $K_{O_2}^{satur}$ ), flux of calcium carbonate ( $f_{CaCO_3}$ ), and maximal phosphorus adsorption capacity of the sediments ( $Q_{max}$ ). The sensitivity ranking of the equilibrium constant of siderite  $K_{eq,FeCO_3,num}$  and calcium carbonate flux ( $f_{CaCO_3}$ ) underscores the importance of the Ca-bound form of phosphorus in the fate of P in the sediments. Close to the latter factor were the parameters for calcium carbonate dissolution ( $k_{eqCaCO_3,diss}$ ), fraction of the settled inorganic iron ( $\alpha_{Inorg\_Fe\_Other}$ ) and bioirrigation coefficient ( $\alpha_{Bioirrig}$ ). This finding is on par with the empirical evidence that apatite P is a significant fraction of the phosphorus pool in the sediments of Lake Simcoe (Dittrich et al., 2009; Hiriart-Baer et al., 2011). The significant impact of calcium carbonate flux ( $f_{CaCO_3}$ ) on modeled outputs stems from the dominance of the Ca-bound form of phosphorus in the sediments. A critical question arising though is whether apatite P directly enters the system from the watershed or if it is being formed in the water column and subsequently settles down to the lake bottom.

#### 4.4. Parameters with low sensitivity ranking

Lower sensitivity rankings were assigned to the rate of compaction ( $k_{\theta}$ ), the nitrification rate ( $k_{nitri}$ ), the concentration of calcium at the sediment–surface interface ( $S_{Ca}^{SWI}$ ), the rate of secondary reaction ( $k_{oxiHS}$ ), and the rate constant of OM degradation with manganese oxides ( $k_{MnO_2}$ ). Likewise, model outputs are less sensitive to the values assigned to dissolved iron concentrations at the sediment–water interface ( $S_{Fe}^{SWI}$ ), adsorption of P ( $K_{Adsorb}$ ), half-saturation constant of OM degradation with iron hydroxides ( $K_{FeOOH}^{satur}$ ), and rate constants of OM degradation with nitrate ( $k_{NO_3}$ ), boundary conditions for concentrations of dissolved manganese ( $S_{Mn}^{SWI}$ ), HS ( $S_{HS}$ ) at the sediment–water interface, half saturation constant of OM degradation with nitrate ( $K_{NO_3}^{satur}$ ), rate of OM degradation with iron hydroxides ( $k_{FeOOH}$ ), parameter for formation of apatite P ( $K_{eqApatite}$ ), sedimentation flux of manganese oxides ( $f_{MnO_2}$ ), half-saturation constants of OM degradation with manganese oxides ( $K_{MnO_2}^{satur}$ ), and kinetics of redox sensitive P ( $k_{Fe-P}$ ). These findings are on par with our empirical calculations of the organic carbon mineralization rates, suggesting that organic carbon is almost 90% mineralized by oxygen in the sediment depths considered in this study (Dittrich et al., 2013). Similar observations have been made in the Baltic Sea, where the majority of mineralization is mediated by aerobic respiration with the maximum occurring shortly after the deposition of the spring bloom, when both labile organic matter and oxygen are readily available (Reed et al., 2011b).

#### 4.5. Identifiability analysis

In this study, our aim was to elucidate the identification problems arising from the compensation effects among different subsets of parameters. The compensation effects can be deduced from the collinearity index  $\gamma$  among the investigated parameters. When the index  $\gamma$  lies below a critical level of 10–20, then the interactions among the parameters do not severely limit their identifiability. Although there is an extremely high number of parameter combinations that can be formed, the  $\gamma$  index is expected to reach a maximum value after a certain parameter subset size. Identifiability studies showed that the maximum collinearity index increases very rapidly with the size of the parameter set. Thus, applications of identifiability analysis can examine relatively low parameter set sizes without losing much information (Omlin et al., 2001). For example, Omlin et al. (2001) found that the collinearity index increased up to 9.2 for parameter subsets of size 2, to 17.0 for parameter subsets of size 3, and to 18.1 for parameter subsets of size 4. This result also implies that despite the large amount of

calibration data in that study, there were already sets of three parameters that led to serious identifiability problems. In our study, we tested 35 different parameter sets and 22 (the most typical ones) are presented (Table 6, 1a–7c). The parameters have been grouped according to their origin and their sensitivity ranking (Table 5). The parameters are divided among those estimated experimentally or supported by available measurements and those estimated solely through calibration (Brun et al., 2001). A second criterion to divide the parameters is their sensitivity ranking in Table 5. The two groups of parameters have been cross-examined in different parameter permutations, in which highly ranked “field measured” parameters, e.g.,  $S_{O_2}$ , and highly ranked “estimated” parameters, e.g.,  $k_{degFe-P}$ , were grouped together to test their identifiability.

The first five parameter sets, 1a–e, in Table 6 with a collinearity index  $\gamma$  below 10–20 suggest the absence of compensation effects among the process rate constants for the degradation with oxygen ( $k_{O_2}$ ), degradation rates of redox sensitive P ( $k_{degFe-P}$ ), rate of formation of redox sensitive P ( $k_{Fe-P}$ ) (sets 1a, b), as well as the nitrification rates ( $k_{nitri}$ ), rate of OM degradation with nitrate ( $k_{NO_3}$ ) (sets 1c, d), manganese oxides ( $k_{MnO_2}$ ) and iron hydroxides ( $k_{FeOOH}$ ) (sets 1e, f). The results for the sets 1a–b demonstrate that the process rates of formation and degradation of redox sensitive phosphorus ( $k_{Fe-P}$  and  $k_{degFe-P}$ ) could be identified simultaneously with the rates of OM degradation with oxygen ( $k_{O_2}$ ). Although the addition of the nitrification rate ( $k_{nitri}$ ) and the rate constant of OM degradation with nitrate ( $k_{NO_3}$ ) leads to an increase of the collinearity index to 3.98 or 4.08 (parameter sets 1c, d), the actual value still stays within the range that suggests minimal compensability problems among the parameters considered. The inclusion of two more rate constants for OM degradation with manganese oxide ( $k_{MnO_2}$ ) and iron hydroxide ( $k_{FeOOH}$ ) leads to an increase of the collinearity index to 10.04 (parameter set 1e). The subsequent consideration of the formation rate for redox sensitive P ( $k_{Fe-P}$ ) increases the collinearity index  $\gamma$  to 14.39, which gets close to the upper limit of the acceptable identifiability range (Brun et al., 2001). Consequently, our study suggests that the available empirical information on phosphorus binding forms and basic sediment

characteristics is adequate for achieving a robust identification of a substantial number of parameters.

The parameter set 2a clearly demonstrates that the ratios of degradable and inert organic matter ( $\alpha_{Org}$ ,  $\alpha_{Org\_inert}$ ) in the sedimentation flux have no compensation problems and can be identified from our calibration dataset. Inclusion of the two rates for OM degradation with oxygen ( $k_{O_2}$ ) and nitrate ( $k_{NO_3}$ ) increases  $\gamma$  to 6.88, which suggests that all of the four parameters are still identifiable (set 2b). However, when we consider the parameters for iron sedimentation flux ( $\alpha_{Inorg\_Fe\_Other}$ ) and redox sensitive P sedimentation flux ( $\alpha_{Inorg\_Fe-P}$ ), an identification problem arises as the collinearity index  $\gamma$  (17.63) gets close to the critical value (2c set). This means that the ratios of degradable and inert organic matter components ( $\alpha_{Org}$ ,  $\alpha_{Org\_inert}$ ) and OM degradation rates with oxygen ( $k_{O_2}$ ) and nitrate ( $k_{NO_3}$ ) may compensate any changes in the values assigned to the redox sensitive P and Fe sedimentation fluxes. This finding underscores the importance of having data on Fe and redox sensitive P flux, if we aim to delineate their actual role in the predictive statements drawn by the model relative to the OM composition and degradation with  $O_2$  and  $NO_3$ .

Combining the rates of the primary degradation with oxygen ( $k_{O_2}$ ), nitrate ( $k_{NO_3}$ ), manganese oxides ( $k_{MnO_2}$ ), iron hydroxides ( $k_{FeOOH}$ ) and secondary degradation process of nitrification, the degradation rate for redox sensitive P ( $k_{degFe-P}$ ) along with the ratios of degradable and refractory organic matter in the sedimentation flux ( $\alpha_{Org}$ ,  $\alpha_{Org\_inert}$ ) into the parameter set 3b (set 3a is the same as set 1e) results in a collinearity index that is far beyond the critical values. The results demonstrate that the rate constants for OM primary degradation processes, rate constant for nitrification and the formation of redox sensitive P can be identified from our data. However, when we also consider the part of organic degradable and refractory matter in the sedimentation flux, the distinct characterization of the parameters included in the set 3b is compromised, leading to the conclusion that it is crucial to have experimental data on the composition of the sedimentation flux and the iron and manganese speciation in the sediments.

In agreement with the sensitivity analysis, the boundary conditions for  $O_2$  and pH ( $S_H^{SWI}$ ) (parameter set 4a) at the sediment–water interface have no identification problems ( $\gamma = 1.65$ ); the addition of a parameter for the P adsorption capacity ( $Q_{max}$ ) did not impact the collinearity index (set 4b). The inclusion of nitrate ( $S_{NO_3}^{SWI}$ ) and bicarbonate ( $S_{HCO_3}^{SWI}$ ) concentrations at the sediment–water interface (parameter sets 4c, d) increases  $\gamma$  to a value beyond the critical values, reflecting the fact that the existing empirical information is not adequate to properly constrain the model. The parameter set 5a demonstrates the absence of identification problems for  $S_{O_2}^{SWI}$  and pH ( $S_H^{SWI}$ ) at the sediment–water interface, the rate constants for OM degradation with oxygen ( $k_{O_2}$ ) and nitrate ( $k_{NO_3}$ ), and the ratios of degradable and inert portions of organic matter ( $\gamma = 9.18$ ). Inclusion of the nitrate ( $S_{NO_3}^{SWI}$ ) and bicarbonate ( $S_{HCO_3}^{SWI}$ ) concentrations at the sediment–water interface result in a  $\gamma$  value of 34.91 (set 5b), stressing the need to study the associated processes in the field; namely, denitrification and calcium carbonate dissolution.

The parameter sets (6a) and (6b) showed that the rates of OM degradation with oxygen ( $k_{O_2}$ ), nitrate ( $k_{NO_3}$ ), nitrification rate ( $k_{nitri}$ ), and the degradation of redox sensitive phosphorus ( $k_{Fe-P}$ ) could be identified ( $\gamma = 3.98$ ). When the constant for carbonate dissolution ( $k_{eqCaCO_3diss}$ ) was added, the collinearity index slightly increased to  $\gamma = 4.73$ . This finding highlights the value of data regarding the calcium-carbonate system at the sediment–water interface.

The parameter set 7a demonstrates that the half-saturation concentrations of OM degradation with oxygen ( $K_{O_2}^{satur}$ ), nitrate ( $K_{NO_3}^{satur}$ ), manganese oxides ( $K_{MnO_2}^{satur}$ ), iron hydroxides ( $K_{FeOOH}^{satur}$ ), parameters for adsorption P ( $K_{Adsorb}$ ) and precipitation constant of siderite ( $K_{eqFeCO_3}$ ) can be identified. The same conclusion holds true when we add the parameter for apatite P formation ( $K_{eqApatite}$ ) (parameter set 7b). However, the inclusion of OM degradation rates with oxygen ( $k_{O_2}$ ), nitrate ( $k_{NO_3}$ ), iron hydroxide ( $k_{FeOOH}$ ), manganese oxides

**Table 6**  
Collinearity indices for selected parameter subsets.

| Set | $\theta$ (sets)   | $\gamma$ ( $\theta$ ) |
|-----|---|-----------------------|
| 1a  |   | 1.03                  |
| 1b  | $k_{O_2}$   | 1.23                  |
| 1c  | $k_{O_2}$ $k_{degFe-P}$   | 3.98                  |
| 1d  | $k_{O_2}$ $k_{degFe-P}$ $k_{nitri}$   | 4.08                  |
| 1e  | $k_{O_2}$ $k_{degFe-P}$ $k_{nitri}$ $k_{NO_3}$  | 10.04                 |
| 1f  | $k_{O_2}$ $k_{degFe-P}$ $k_{nitri}$ $k_{NO_3}$ $k_{MnO_2}$ $k_{FeOOH}$                | 14.39                 |
| 2a  |   | 1.99                  |
| 2b  | $\alpha_{Org\_inert}$ $\alpha_{Org}$  | 6.88                  |
| 2c  | $\alpha_{Org\_inert}$ $\alpha_{Org}$ $k_{O_2}$  | 17.73                 |
| 3a  | $k_{O_2}$ $k_{degFe-P}$ $k_{nitri}$   | 10.04                 |
| 3b  | $k_{O_2}$ $k_{degFe-P}$ $k_{nitri}$ $k_{NO_3}$ $k_{MnO_2}$ $k_{FeOOH}$                | 98.30                 |
| 4a  |   | 1.65                  |
| 4b  |   | 1.65                  |
| 4c  | $S_{O_2}^{SWI}$ $S_H^{SWI}$   | 22.52                 |
| 4d  | $S_{O_2}^{SWI}$ $S_H^{SWI}$ $Q_{max}$   | 28.23                 |
| 5a  | $S_{O_2}^{SWI}$ $S_H^{SWI}$ $k_{O_2}$   | 9.18                  |
| 5b  | $S_{O_2}^{SWI}$ $S_H^{SWI}$ $k_{O_2}$ $k_{NO_3}$ $\alpha_{Org\_inert}$ $\alpha_{Org}$ | 34.91                 |
| 6a  | $k_{O_2}$ $k_{NO_3}$ $k_{nitri}$  | 3.98                  |
| 6b  | $k_{O_2}$ $k_{NO_3}$ $k_{nitri}$ $k_{Fe-P}$   | 4.73                  |
| 7a  | $K_{eqFeCO_3}$ $K_{O_2}$ $K_{FeOOH}$ $K_{NO_3}$ $K_{Ads}$                             | 3.11                  |
| 7b  | $K_{eqFeCO_3}$ $K_{O_2}$ $K_{FeOOH}$ $K_{NO_3}$ $K_{Ads}$                             | 4.74                  |
| 7c  | $K_{eqFeCO_3}$ $K_{O_2}$ $K_{FeOOH}$ $K_{NO_3}$ $K_{Ads}$                             | 98.12                 |

( $k_{\text{MnO}_2}$ ) along with the formation rate for redox sensitive P ( $k_{\text{Fe-P}}$ ) significantly increases the collinearity index, and thus the 13 parameters together cannot be identified from the available data set.

To put our results into perspective, identifiability studies for biogeochemical lake (Omlin et al., 2001) and river water quality models (Reichert and Vanrolleghem, 2001) reported approximately the same number of identifiable parameters. On the other hand, the analysis of a diagenesis model with significantly more data available showed a greater number of identified parameters (Dittrich et al., 2009). In a non-steady-state diagenetic modeling study in Lake Zug (Dittrich et al., 2009), 27 parameters have been found to be identifiable compared to 7 identifiable parameters in the present study (set 1f). A plausible explanation lies in the availability of experimental data to calibrate the model and therefore to effectively determine model parameters. While in the Lake Zug study, a four-year seasonal data set on sediment geochemistry was available, the present study only used two years of field data to build the basics for the model calibration (Dittrich et al., 2009).

It should be noted that the identifiability of model parameters does not guarantee ecologically sound values. Biases in the model parameterization can not only stem from parameters that are not identified from the data, but also from the deficiencies in the model structure and mathematical foundation. In our study, the most important parameters are the rates for OM degradation with oxygen ( $k_{\text{O}_2}$ ) and nitrate ( $k_{\text{NO}_3}$ ), oxygen and pH  $\text{S}_{\text{O}_2}^{\text{SWI}}$ ,  $\text{S}_{\text{H}}^{\text{SWI}}$ , and degradation of redox sensitive P ( $k_{\text{degFe-P}}$ ). Our sensitivity and identifiability analysis exercise highlighted the significance of monitoring the calcium-carbonate system in the sediments for the diagenesis of phosphorus in hard-water lakes. Furthermore, the data on the dynamics and composition of the sedimentation fluxes, especially organic carbon, and the portion of redox-sensitive phosphorus, are of great importance. Measured depth profiles of phosphorus binding forms and organic matter provide a large amount of information on phosphorus diagenesis. Consequently, the rates of redox sensitive P degradation ( $k_{\text{degFe-P}}$ ), sediment P maximum adsorption capacity ( $Q_{\text{max}}$ ) and the rates of apatite P formation ( $K_{\text{eqApatite}}$ ) can be estimated accurately. In summary, the identifiability analysis clearly showed that the majority of our model parameters can be reasonably identified, supporting the likelihood of achieving robust predictions on phosphorus fluxes and dynamics of phosphorus binding forms at the sediment surface.

## 5. Conclusions

In the present study, we developed a dynamic reaction-transport model for P transformation and retention in lake sediments. We also integrated limnological historical data on sedimentation rates and oxygen in the deep water of the lake as boundary conditions. The model reproduced depth profiles of phosphorus binding forms, solid-phase, pore-water, and sediment–water interface concentrations during the mid-spring and early fall period in three basins of the mesotrophic, hard-water Lake Simcoe.

The non-steady state diagenesis model reveals that apatite P dominates the P forms in Cook's Bay, which has been overwhelmingly influenced by agricultural activities in the corresponding watershed during the last 100 years. In contrast, Kempenfelt Bay has been primarily impacted by urbanization and experienced oxygen depletion in the deep water. Thus, we found that organic P binding forms dominated over redox sensitive P when urban loading intensified. Furthermore, we quantified the seasonal dynamics of benthic P fluxes into the water column in three different basins and tracked the phosphorus binding forms in the surface sediments over 200 years. The model reasonably quantified the historical P fluxes to and from the sediments, and thus can be used as a predictive tool to support the quantification of lake P budgets under different loading and oxygen conditions.

Our findings indicate that Lake Simcoe experiences internal loading that may be causing an increase of primary production as well as a disconnect between external loading and system response (Winter et al.,

2007; Hiriart-Baer et al., 2011). This result is also in agreement with the evidence of P accumulation in the deep lake waters (Nürnberg et al., 2013). Our analysis also demonstrated that the model outputs are sensitive to the concentrations of dissolved oxygen and pH at the sediment–water interface. The sensitivity with respect to these factors overwhelmingly dominates over all other parameters. Furthermore, the characterization of the sedimentation fluxes is the second strongest factor that can influence the inference drawn by the model; namely, the composition of settling organic matter, reflected as the ratio of degradable and inert organic matter.

Because of the substantial empirical information on P binding forms and associated conditions at the sediment–water interface ( $\text{O}_2$  and pH), we were able to achieve remarkable identifiability for a large number of model parameters and P diagenesis processes. For most parameters, we can expect that the satisfactory identification can lead to mechanistically plausible values and consequently to predictive statements that are based upon an ecologically robust foundation. However, we caution that some uncertainty still remains in regard to the sedimentation fluxes of iron hydro-oxides and manganese oxides, as those compounds were not measured.

Generally, our study demonstrated that the P binding forms in the sediments are indicators of the prevailing lake redox conditions and the total nutrient inflows from the watershed. Simulations of phosphorus binding forms in surface sediments offer a quantitative interpretation of paleo-limnological data and thus dictate a new perspective into assessing lake P retention and linking land use patterns with sediment P concentrations. In principle, our attempt to recreate the trajectory from the oligotrophic state 400 years ago to the current mesotrophic conditions, can be more broadly used to achieve model-based reconstructions of environmental change. From a water management point of view, the model creates a virtual environment for evaluating organic matter degradation pathways and oxygen demand regimes, once the boundary conditions and sediment characteristics are sufficiently described. In this regard, our model provides a process-based platform for assessing management strategies and making decisions regarding hypoxia problems in aquatic systems. In a follow-up study, we are investigating the interplay between changing sedimentation rates and oxygen depletion in the deep waters of the lake.

Supplementary data to this article can be found online at <http://dx.doi.org/10.1016/j.chemgeo.2013.06.011>.

## Acknowledgments

This project was undertaken with the financial support of the Government of Canada provided through the Department of the Environment (Lake Simcoe Clean-up Fund) and the University of Toronto (start-up funding to Maria Dittrich). Alex Gudimov received financial support from a NSERC doctoral award and an Ontario Graduate Scholarship.

## References

- Arhonditsis, G.B., Brett, M.T., 2004. Evaluation of the current state of mechanistic aquatic biogeochemical modelling. *Marine Ecology-Progress Series* 271, 13–26.
- Bostrom, B., Persson, G., Bromberg, B., 1988. Bioavailability of different phosphorus forms in freshwater systems. *Hydrobiologia* 170, 133–135.
- Boudreau, B.P., 1997. *Diagenetic Models and Their Implementation: Modelling Transport and Reactions in Aquatic Sediments*. Springer, Berlin.
- Belsley, D.A., 1991. *Conditioning Diagnostics – Collinearity and Weak Data in Regression*. Wiley, New York.
- Belsley, D.A., Kuh, E., Welsch, R.E., 1980. *Regression Diagnostics – Identifying Influential Data and Sources of Collinearity*. Wiley, New York.
- Brun, R., Reichert, P., Kunsch, H.R., 2001. Practical identifiability analysis of large environmental simulation models. *Water Resources Research* 37 (4), 1015–1030.
- Carey, C.C., Rydin, E., 2011. Lake trophic status can be determined by the depth distribution of sediment phosphorus. *Limnology and Oceanography* 56 (6), 2051–2063.
- Christophoridis, C., Fytianos, K., 2006. Conditions affecting the release of phosphorus from surface lake sediments. *Journal of Environmental Quality* 35 (4), 1181–1192.

- Clegg, S., Whitfield, M., 1995. A chemical model of seawater including dissolved ammonia and the stoichiometric dissociation constant of ammonia in estuarine water and seawater from  $-2$  to  $40$  °C. *Geochimica et Cosmochimica Acta* 59 (12), 2403–2421.
- Couture, R.M., Shafei, B., Van Cappellen, P., Tessier, A., Gobeil, C., 2010. Non-steady state modelling of arsenic diagenesis in lake sediments. *Environmental Science and Technology* 44 (1), 197–203.
- Couture, R.M., Van Cappellen, P., 2011. Reassessing the role of sulfur geochemistry on arsenic speciation in reducing environments. *Journal of Hazardous Materials* 189 (3), 647–652.
- Draper, N.R., Smith, H., 1998. *Applied Regression Analysis* Third ed. Wiley, New York.
- Dittrich, M., Wehri, B., Reichert, P., 2009. Lake sediments during the transient eutrophication period: reactive-transport model and identifiability study. *Ecological Modelling* 220 (20), 2751–2769.
- Dittrich, M., Gabriel, O., Rutzan, C., Koschel, R., 2011. Lake restoration by hypolimnetic  $\text{Ca}(\text{OH})_2$  treatment: impact on phosphorus sedimentation and release from sediment. *Science of the Total Environment* 409 (8), 1504–1515.
- Dittrich, M., Chesnyuk, A., Gudimov, A., McCulloch, J., Quaizi, S., Young, J., Winter, J., Stainsby, E., Arhonditsis, G.B., 2013. Phosphorus retention in a mesotrophic lake under transient loading conditions: insight from sediment phosphorus binding form studies. *Water Research* 47, 1433–1447.
- Dong, L., Yang, Z., Liu, X., 2011. Phosphorus fractions, sorption characteristics, and its release in the sediments of Baiyangdian Lake, China. *Environmental Monitoring and Assessment* 179, 335–345.
- Evans, D.O., 2007. Effects of hypoxia on scope-for-activity and power capacity of lake trout (*Salvelinus namaycush*). *Canadian Journal of Fisheries and Aquatic Sciences* 64 (2), 345–361.
- Falkowski, P., Scholes, R., Boyle, E., Canadell, J., Canfield, D., Elser, J., Gruber, N., Hibbard, K., Höglberg, P., Linder, S., 2000. The global carbon cycle: a test of our knowledge of earth as a system. *Science* 290 (5490), 291–296.
- Gao, L., Zhou, J.M.M., Yang, H., Chen, J., 2005. Phosphorus fractions in sediment profiles and their potential contributions to eutrophication in Dianchi Lake. *Environmental Geology* 48 (7), 835–844.
- Gear, C.W., 1971. *Numerical Initial Value Problems in Ordinary Differential Equations*. Prentice Hall, Englewood Cliffs.
- Gonsiorczyk, T., Casper, P., Koschel, R., 1998. Phosphorus-binding forms in the sediment of an oligotrophic and an eutrophic hardwater lake of the Baltic lake district (Germany). *Wat. Sci. Res.* 37, 51–58.
- Graneli, W., 1999. Internal phosphorus loading in Lake Ringsjön. *Hydrobiologia* 404, 19–26.
- Gudimov, A., O'Connor, E., Dittrich, M., Jarjanazi, H., Palmer, M.E., Stainsby, E.A., Winter, J.G., Young, J.D., Arhonditsis, G.B., 2012. Continuous Bayesian network for studying the causal links between phosphorus loading and plankton patterns in Lake Simcoe, Ontario, Canada. *Environmental Science and Technology* 46 (13), 7283–7292.
- Hiriart-Baer, V.P., Milne, J.E., Marvin, C.H., 2011. Temporal trends in phosphorus and lacustrine productivity in Lake Simcoe inferred from lake sediment. *Journal of Great Lakes Research* 37 (4), 764–771.
- House, W.A., 1990. The prediction of phosphate coprecipitation with calcite in freshwater. *Water Research* 24 (8), 1017–1023.
- Hupfer, M., Gächter, R., Giovanoli, R., 1995. Transformation of phosphorus species in settling seston and during early sediment diagenesis. *Aquatic Sciences* 57 (4), 305–324.
- Hupfer, M., Lewandowski, J., 2008. Oxygen controls the phosphorus release from lake sediments—a long-lasting paradigm in limnology. *International Review of Hydrobiology* 93 (4–5), 415–432.
- Johnson, M.G., Nicholls, K.H., 1989. Temporal and spatial variability in sediment and phosphorus loads to Lake Simcoe, Ontario. *Journal of Great Lakes Research* 15 (2), 265–282.
- Jourabchi, P., Van Cappellen, P., Regnier, P., 2005. Quantitative interpretation of pH distributions in aquatic sediments: a reaction-transport modelling approach. *American Journal of Science* 305 (9), 919–956.
- Katsev, S., Tsandev, I., L'Heureux, I., Rancourt, D.G., 2006. Factors controlling long-term phosphorus efflux from lake sediments: exploratory reactive-transport modelling. *Chemical Geology* 234 (1–2), 127–147.
- Klausmeier, C.A., Litchman, E., Daufresne, T., Levin, S.A., 2004. Optimal nitrogen-to-phosphorus stoichiometry of phytoplankton. *Nature* 429 (6988), 171–174.
- Kleeberg, A., Kozerski, H.P., 1997. Phosphorus release in Lake Großer Müggelsee and its implications for lake restoration. *Hydrobiologia* 342 (343), 9–26.
- Kopacek, J., Borovec, J., Hejzlar, J., Ulrich, K.U., Norton, S.A., Amirbahman, A., 2005. Aluminum control of phosphorus sorption by lake sediments. *Environmental Science & Technology* 39 (22), 8784–8789.
- Koschel, R., Benndorf, J., Proft, G., Recknagel, F., 1983. Calcite precipitation as a natural control mechanism of eutrophication. *Archives of Hydrobiology* 98, 380–408.
- Landre, A.L., Winter, J.G., Helm, P., Hiriart-Baer, V., Young, J., 2011. Metals in Lake Simcoe sediments and tributaries: do recent trends indicate changing sources? *Journal of Great Lakes Research* 37, 124–131.
- Lewandowski, J., Ruter, K., Hupfer, M., 2002. Two-dimensional small-scale variability of pore water phosphate in freshwater lakes: results from a novel dialysis sampler. *Environmental Science and Technology* 36 (9), 2039–2047.
- Lewis, G.N., Auer, M.T., Xiang, X.Y., Penn, M.R., 2007. Modelling phosphorus flux in the sediments of Onondaga Lake: insights on the timing of lake response and recovery. *Ecological Modelling* 209 (2–4), 121–135.
- Lopes, F., Michard, G., Poulin, M., Roue, A., Prévot, F., Jézéquel, D., Viollier, E., 2010. Biogeochemical modelling of a seasonally anoxic lake: calibration of successive and competitive pathways and processes in Lake Aydat, France. *Aquatic Geochemistry* 16 (4), 587–610.
- LSRCA, 1993. *Estimation of Phosphorus Loadings and Evaluation of Empirical Oxygen Models for Lake Simcoe for 1970–1990*. Lake Simcoe Region Conservation Authority.
- Lukkari, K., Hartikainen, H., Leivuori, M., 2007. Fractionation of sediment phosphorus revisited. I: fractionation steps and their biogeochemical basis. *Limnology and Oceanography—Methods* 5, 433–444.
- MOE, 2008. *Lake Simcoe Water Quality Executive Summary*. Lake Simcoe Project Team. Ministry of the Environment.
- MOE, 2010. *Lake Simcoe water quality update*. Report to the Minister of the Environment.
- Nicholls, K.H., 1995. Some recent water quality trends in Lake Simcoe, Ontario: implications for basin planning and limnological research. *Canadian Water Resources Journal* 20 (4), 213–226.
- Nürnberg, G.K., 1988. Prediction of phosphorus release rates from total and reductant-soluble phosphorus in anoxic lake sediments. *Canadian Journal of Fisheries and Aquatic Sciences* 45, 453–462.
- Nürnberg, G.K., 2009. Assessing internal phosphorus load—problems to be solved. *Lake and Reservoir Management* 25 (4), 419–432.
- Nürnberg, G.K., Molot, L.A., O'Connor, E., Jarjanazi, H., Winter, J., Young, J., 2013. Evidence for internal phosphorus loading, hypoxia and effects on phytoplankton in partially polymictic Lake Simcoe, Ontario. *Journal of Great Lakes Research* 39, 259–270.
- Omlin, M., Brun, R., Reichert, P., 2001. Biogeochemical model of Lake Zurich: sensitivity, identifiability and uncertainty analysis. *Ecological Modelling* 141 (1–3), 105–123.
- Palmer, M.E., Winter, J.G., Young, J.D., Dillon, P.J., Guildford, S.J., 2011. Introduction and summary of research on Lake Simcoe: research, monitoring, and restoration of a large lake and its watershed. *Journal of Great Lakes Research* 37, 1–6.
- Petzold, L., 1983. In: Stepleman, R., et al. (Ed.), *Scientific Computing*. IMACS, North-Holland, pp. 65–68.
- Psenner, R., Pusco, R., 1988. Phosphorus fractionation: advantages and limits of the method for the study of sediment P origins and interactions. *Arch. Hydrobiol. Beih.* 30, 43–59.
- Reed, D.C., Slomp, C.P., de Lange, G.J., 2011a. A quantitative reconstruction of organic matter and nutrient diagenesis in Mediterranean Sea sediments over the Holocene. *Geochimica et Cosmochimica Acta* 75 (19), 5540–5558.
- Reed, D.C., Slomp, C.P., Gustafsson, B.G., 2011b. Sedimentary phosphorus dynamics and the evolution of bottom-water hypoxia: a coupled benthic–pelagic model of a coastal system. *Limnology and Oceanography* 56 (3), 1075–1092.
- Reichert, P., 1994. Aquasim — a tool for simulation and analysis of aquatic systems. *Water Science and Technology* 2 (30), 21–30.
- Reichert, P., 1995. Design techniques of a computer-program for the identification of processes and the simulation of water-quality aquatic systems. *Environmental Software* 10 (3), 199–210.
- Reichert, P., Vanrolleghem, P., 2001. Identifiability and uncertainty analysis of the River Water Quality Model No. 1 (RWQM1). *Water Science and Technology* 43 (7), 329–338.
- Rydin, E., 2000. Potentially mobile phosphorus in Lake Erken sediment. *Water Research* 34 (7), 2037–2042.
- Schauser, I., Lewandowski, J., Hupfer, M., 2003. Decision support for the selection of an appropriate in-lake measure to influence the phosphorus retention in sediments. *Water Research* 37 (4), 801–812.
- Schindler, D.W., Hecky, R., Findlay, D., Stainton, M., Parker, B., Paterson, M., Beaty, K., Lyng, M., Kasian, S., 2008. Eutrophication of lakes cannot be controlled by reducing nitrogen input: results of a 37-year whole-ecosystem experiment. *Proceedings of the National Academy of Sciences* 105 (32), 11254–11258.
- Schippers, P., Van de Weerd, H., De Klein, J., De Jong, B., Scheffer, M., 2006. Impacts of agricultural phosphorus use in catchments on shallow lake water quality: about buffers, time delays and equilibria. *Science of the Total Environment* 369 (1), 280–294.
- Smith, L., Watzin, M.C., Druschel, G., 2011. Relating sediment phosphorus mobility to seasonal and diel redox fluctuations at the sediment water interface in a eutrophic freshwater lake. *Limnology and Oceanography* 56 (6), 2251–2264.
- Stantec, 2006. *Benthic macro-invertebrate sampling and analysis of Lake Simcoe*. Final Report: Prepared for Lake Simcoe Region Conservation Authority.
- Stumm, W., Morgan, J., 1996. *Aquatic Chemistry. An Introduction Emphasizing Chemical Equilibria in Natural Waters*. John Wiley & Sons, New York.
- Todd, B.J., Lewis, C.F.M., Anderson, T.W., 2008. Quaternary features beneath Lake Simcoe, Ontario, Canada: drumlins, tunnel channels, and records of pro-glacial to postglacial closed and overflowing lakes. *Paleolimnol* 39, 361–380.
- Ulrich, K.U., 1997. Effects of land use in the drainage area on phosphorus binding and mobility in the sediments of four drinking-water reservoirs. *Hydrobiologia* 345 (1), 21–38.
- Van Cappellen, P., Gaillard, J.-F., 1996. In: Lichtner, P.C., Steefel, C.I., Oelkers, E.H. (Eds.), *Reactive Transport in Porous Media*. The Mineralogical Society of America, pp. 335–376.
- Wetzel, R., 2001. *Limnology, Lake and River Ecosystems*. Academic Press, USA.
- Winter, J.G., Eimers, M.C., Dillon, P.J., Scott, L.D., Scheider, W.A., Wilcox, C.C., 2007. Phosphorus inputs to Lake Simcoe from 1990 to 2003: declines in tributary loads and observations on lake water quality. *Journal of Great Lakes Research* 33 (2), 381–396.
- Young, J.D., Winter, J.G., Molot, L., 2011. A re-evaluation of the empirical relationships connecting dissolved oxygen and phosphorus loading after dreissenid mussel invasion in Lake Simcoe. *Journal of Great Lakes Research* 37, 7–14.
- Zhou, A., Tang, H., Wang, D., 2005. Phosphorus adsorption on natural sediments: modelling and effects of pH and sediment composition. *Water Research* 39 (7), 1245–1254.

Supplementary Material Table 1. Values of scaling factors  $sc_i$

| $y_i$              | $sc_i$               |        |
|--------------------|----------------------|--------|
| $S_{O_2}$          | 0.219                | mmol/l |
| $S_{Ca}$           | 1                    | mmol/l |
| $S_{CO_3}$         | 0.001                | mmol/l |
| $S_{HPO_4}$        | 0.0009               | mmol/l |
| $S_{NO_3}$         | 0.022                | mmol/l |
| $S_{HS}$           | 0.007                | mmol/l |
| $S_{NH_4}$         | 0.05                 | mmol/l |
| $S_{S_2}$          | $2.4 \cdot 10^{-10}$ | mmol/l |
| $S_{SO_4}$         | 0.03                 | mmol/l |
| $S_{Mn}$           | 0.02                 | mmol/l |
| $S_{Fe}$           | 0.0088               | mmol/l |
| pH                 | 8.19                 |        |
| $X_{orgfast}$      | 35                   | mg/gDM |
| $X_{orgine}$       | 10                   | mg/gDM |
| $X_{MnO_2}$        | 1.4                  | mg/gDM |
| $X_{MnCO_3}$       | $3.8 \cdot 10^{-4}$  | mg/gDM |
| $X_{CaCO_3}$       | 2.2                  | mg/gDM |
| $X_{P\_Apatite}$   | 0.44                 | mg/gDM |
| $X_{FeOOH}$        | 151                  | mg/gDM |
| $X_{Fe\_Other}$    | 1.5                  | mg/gDM |
| $X_{P\_Absorbed}$  | 0.16                 | mg/gDW |
| $X_{FeCO_3}$       | $1.7 \cdot 10^{-4}$  | mg/gDW |
| $X_{P\_BD}$        | 0.4                  | mg/gDW |
| $X_{Inorg\_Other}$ | 0.3                  | mg/gDW |